Underground Injection Control – Class VI Permit Application for

High West CCS Project
Spoonbill No. 001 to 005

St. Charles and Jefferson Parishes, Louisiana

SECTION 2 – PLUME MODEL

Prepared for High West Sequestration LLC
Denver, Colorado

By
Lonquist Sequestration, LLC
Austin, Texas

March 2025

LONQUIST

SECTION 2 – PLUME MODEL

TABLE OF CONTENTS

Figures

Tables

2.1 Introduction

In compliance with Statewide Order (SWO) 29-N-6, **§3615.B** [Title 40, U.S. Code of Federal Regulations (40 CFR) **§146.84**], the following discussion centers on the plume model for the High West CCS Project. The model establishes the required pore space, defines the area of review (AOR), outlines comprehensive corrective action plans, and assesses the overall feasibility of the project within the specified regulatory framework. Both *Section 3 – AOR and Corrective Action Plan* and *Section 5 – Testing and Monitoring Plan* utilize the forecasted plume to help determine the best strategies and plans to minimize the impact of carbon sequestration.

The primary objectives of the plume model are to:

1. Maximize the utilization of accessible pore space for carbon sequestration activities.
2. Evaluate the most strategically optimal well locations to facilitate carbon storage.
3. Simulate and assess the migration of injected CO_2 and the resultant pressure influence to prevent any adverse effects on underground sources of drinking water (USDW), critically stressed faults, or other oil and gas, injection, or mining activities.
4. Provide supporting data to determine corrective action and monitoring plans.

2.2 Project Summary

The High West CCS Project site is in St. Charles and Jefferson Parishes, approximately 10 miles (mi) southwest of New Orleans, Louisiana, and 8 mi south of Waggaman, Louisiana. The sequestration site encapsulates 21,079 acres of land that is viable for carbon capture and storage (CCS). The focus of this permit application is on five injection wells, Spoonbill Nos. 001, 002, 003, 004, and 005, where each well plans to inject between 1.5 to 2.5 million metric tons per year (MMT/yr). Each well plans to inject for 20 years, resulting in a total of 30 to 50 MMT of supercritical CO_2 being safely sequestered per well. Throughout the life of the project, a total of 200 MMT will be stored in the High West CCS Project area. Figure A-2 in *Appendix A* provides a detailed description of the property.

2.2.1 Software

2.2.1.1 Petrel™ Software Suite

Industry standard SLB's (previously Schlumberger) Petrel software has been selected for the intricate task of constructing a detailed geocellular model as part of the permit application for the CCS site. This globally recognized software seamlessly integrates data from both well logs and seismic sources to generate a highly accurate representation of the subterranean reservoir. The geocellular model, developed with Petrel, delineates various layers of the site, including the Miocene Shales between Sequence Boundary (SB) 2.1 and SB 2.1B (upper confining zone (UCZ)), Miocene sands from FS 4-SB 7.3 (injection zone), and Miocene shales between SB 7.3 and FS 7.4 (lower confining zone (LCZ)). Utilizing Petrel, the permeability and porosity properties of the injection were spatially distributed, incorporating well log analysis and established methodologies. These approaches enhance the accuracy of the reservoir depiction in the model.

2.2.1.2 Rock Flow Dynamic's Software Suite – tNavigator

The tNavigator software suite offers a comprehensive suite of capabilities for advanced reservoir modeling and simulation, making it a powerful tool across a spectrum of subsurface applications. Its core strengths lie in its high-performance computing architecture, enabling rapid and accurate simulations of complex reservoir behaviors. This architecture includes sophisticated Equation of State (EOS), crucial for predicting the movement of supercritical fluids like CO_2 in CCS projects. The software offers advanced visualization capabilities to provide users with detailed insights into simulation results, helping facilitate informed decision-making. This software can perform sensitivity analysis that allows for robust risk assessment and optimization of field development strategies.

2.2.2 Data Sources

The data sources used to build the geocellular and dynamic models include offset well logs, core data, 3D seismic data, public databases, and publicly available literature, such as the Society of Petroleum Engineers (SPE) and American Association of Petroleum Geologists (AAPG) peer-reviewed papers. Specific references are cited as relevant.

An initial assessment involved the examination of public databases and literature at both regional and site-specific scales. The regional review aimed to discern major trends within the project area and its vicinity. By comparing these trends with site-specific data, an increased confidence level in the reservoir properties was achieved. Utilizing public regional databases was instrumental in estimating the salinity and temperature of the reservoir. Additionally, key reservoir properties such as rock compressibility and relative permeability were deduced from information available in public literature. These assumptions are further discussed in *Section 2.5*.

Offset well log analysis was conducted to inform the reservoir characterization and populate the geocellular model. The openhole log data encompassed comprehensive analyses including gamma ray, spontaneous potential (SP), resistivity, porosity (sonic, neutron, density), photoelectric factor, caliper, and other relevant measurements. Utilizing these well logs enabled the identification of formation tops, determination of rock properties, and assessment of temperature gradients, thereby enhancing the representation of the subsurface reservoir. Petrophysical analysis was performed on 55 wells, shown in Figure 2-1, to appraise the target injection zone and subsequent confining layers.

Figure 2-1 – Map of the data employed for the High West CCS Project , showing the injection site (yellow star), wells with licensed biostratigraphic reports (the red stars), the Waterford Oil Company No. 001 (API No. 17-089-00211, Serial No. 64758) type log (purple star), proposed High West stratigraphic test well location (blue triangle), petrophysics wells (cyan circles), Avondale 3D seismic data (green dashed outline), Gheens 3D seismic data (red dashed outline), Couba Island 3D seismic data (blue dashed outline), and leased property (Blue solid outline).

The High West CCS Project area was covered by several 3D seismic surveys conducted for oil and gas exploration. One hundred square miles of 3D seismic survey data were licensed from three surveys and were processed into one merged 75 mi^2 survey for interpretation. The seismic reprocessing had several goals: 1) process data from the three surveys with a consistent seismic wavelet, 2) use a consistent statics calculation across the three surveys, 3) normalize the surveys to a uniform source-to-receiver azimuth and offset distribution, 4) image the subsurface with a consistent velocity function, and 5) bring all three surveys on to a consistent grid for interpretation. These goals were met which resulted in a unified seismic dataset that was used to fully evaluate subsurface features and formation trends at the High West CCS site.

A comprehensive assessment of the 3D seismic survey data was conducted and seamlessly integrated into the workflow to enhance the characterization of the injection zone and confining layers. The supplementary data acquired from the 3D seismic survey, coupled with the formation tops identified through well-log analysis, was employed for the identification of key structural

horizons, as illustrated in Figure 2-2. The seismic data allowed for an enhanced visualization of the subsurface, revealing features such as faults, structural, or stratigraphic changes in the subsurface. Integrating this data into the geocellular model substantially enhanced its precision, resulting in a more thorough comprehension of the targeted stratigraphy including the Flooding Surfaces (FS) and SBs illustrated in Figure 2-2.

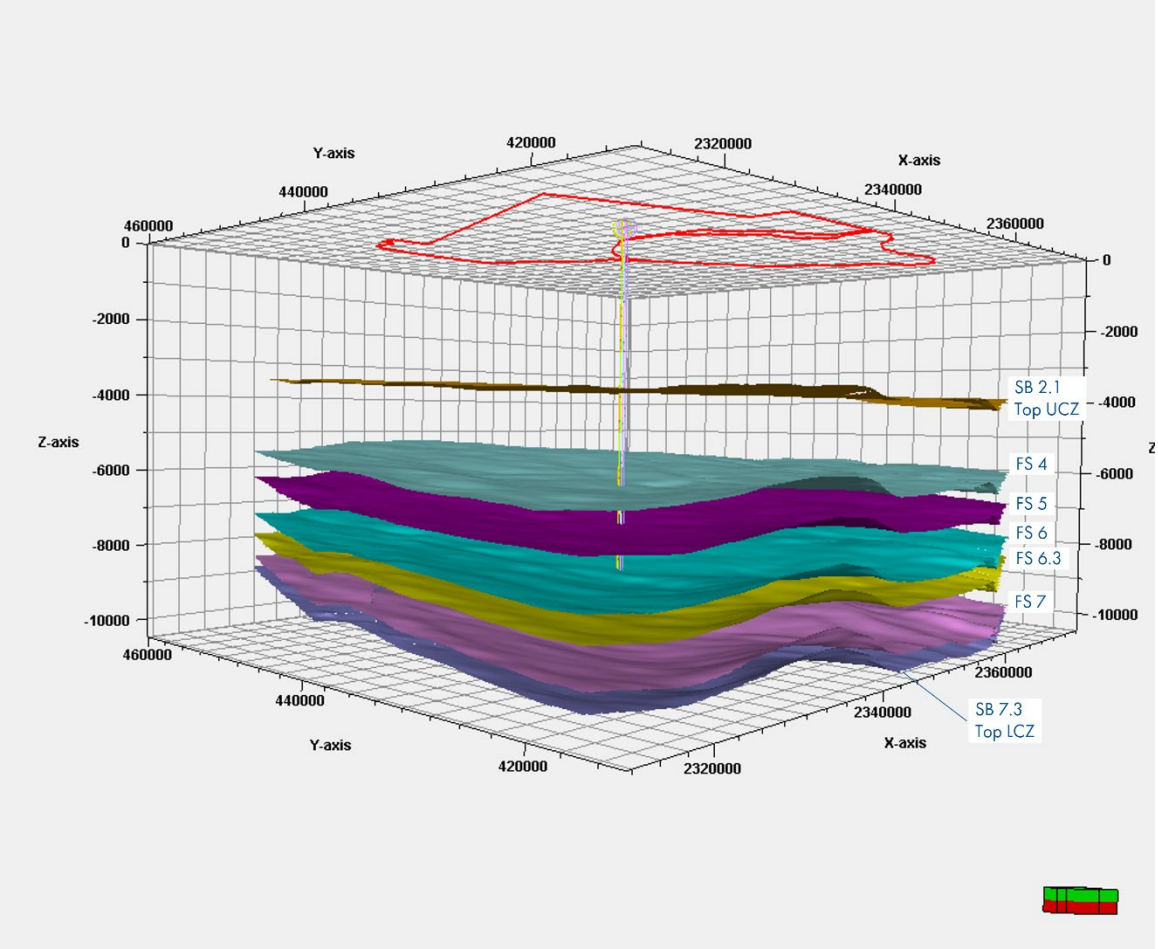

Figure 2-2 – Major structural horizons used in the construction of the static earth model (SEM). Injection will occur across five zones bounded by FS 4 and SB 7.3. The top of the lower confining zone (LCZ) and the upper confining zone (UCZ) are shown as SB 7.3 and SB 2.1, respectively. Vertical exaggeration is 3x.

Additional site-specific data will be collected after the submittal of this permit application to supplement the data and findings that supported the project design work in this submission. A stratigraphic test well is planned to gather core, fluid samples, and geophysical logs, including additional data that will further increase the accuracy of the computational models.

2.3 Trapping Mechanisms

In a CCS project, four primary trapping mechanisms exist that sequester the supercritical CO_2, schematically represented in Figure 2-3. Structural and stratigraphic, residual gas (also referred to as residual CO_2), solubility, and mineral trapping mechanisms—all present in the current model except for mineral trapping—are discussed in the following sections.

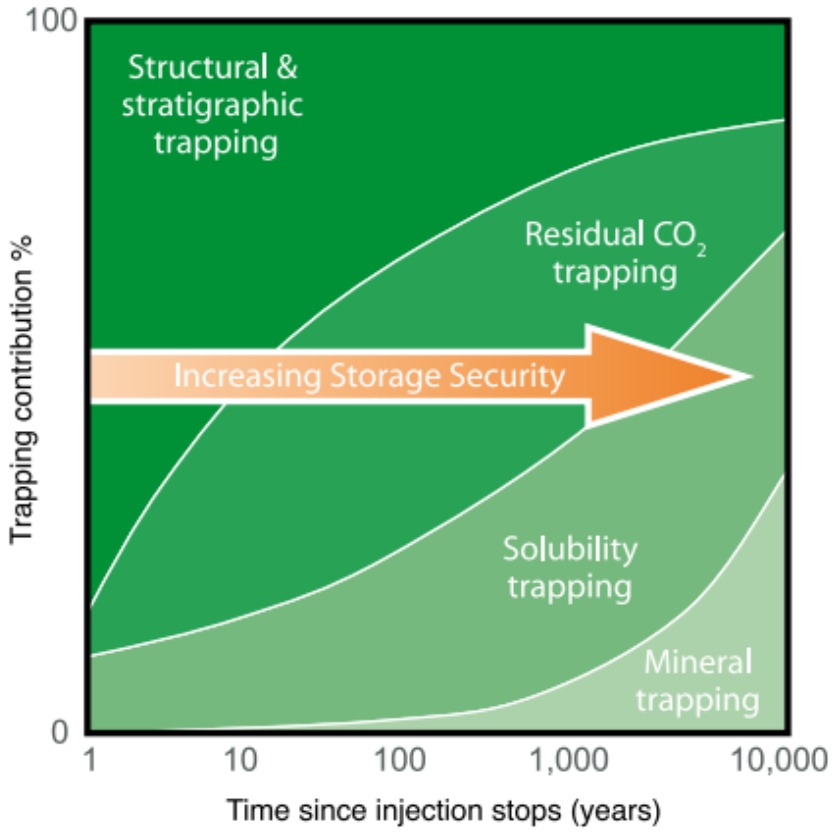

Figure 2-3 – CO_2 Storage Mechanisms (IPCC, 2005)

2.3.1 Structural/Stratigraphic Trapping

Structural trapping in CCS involves the physical confinement of injected CO_2 through the presence of sealing faults, stratigraphic, or other geological traps. Similar to naturally occurring hydrocarbon reservoirs, CO_2 can frequently be sequestered in anticlinal folds. This phenomenon is captured in the geologic model. The static model contains the confining shales and shale baffles that act as barriers inhibiting supercritical CO_2 flow. As a low-viscosity fluid, supercritical CO_2 is less dense than the surrounding brine in the injection zone. Consequently, CO_2 ascends until its buoyant forces are no longer greater than the capillary entry pressure of the caprock. In the dynamic model, the mass density of CO_2 exhibits a range from approximately 45.2 pounds per cubic feet (lb/ft^3), in the shallowest injection interval, to 48.2 lb/ft^3, in the deepest intervals. Concurrently, the average surrounding brine density was calculated at 65.92 lb/ft^3.

EOS calculations are executed to ascertain and predict the phase behavior, density, and other thermodynamic properties of CO_2. These mathematical formulations can predict the density and phase segregation of the injected fluid at any given model location based on the pressure and temperature conditions at that location. tNavigator uses several well-known EOS formulas, including the modified Peng-Robinson method (Peng and Robinson, 1976). The EOS implemented within the plume model was the modified Peng-Robinson method, due to its widely accepted use for volumetric and phase equilibria.

2.3.2 Residual Gas Trapping

Residual gas trapping constitutes a physical trapping mechanism where minute quantities of CO_2 persist in the pore space as the plume continues to migrate. As water is displaced in the rock, the CO_2 fills the space. However, depending on the movement of CO_2 and the aqueous phase through saturation and capillary forces, CO_2 remains residually trapped within the pore space.

Hysteresis modeling is used in the model to accurately predict the amount of residually trapped supercritical CO_2. tNavigator offers several methods to determine residual gas trapping, such as the Carlson and Land model (Land, 1968) (Land, 1971) (Carlson, 1981). The "CARLSON_A" keyword was chosen to implement the Carlson and Land model for this simulation because of (1) it is validated for use in water-alternating-gas injection and (2) it is the one model that represents the two-phase system. The critical parameter—trapped gas saturation—will be discussed in *Section 2.5.3*.

2.3.3 Solubility Trapping

Solubility trapping is a chemical trapping mechanism characterized by the interaction between supercritical CO_2 and brine. Due to its high solubility in brine, CO_2 forms a solution with a higher density than the original connate brine. As a result, the CO_2-laden brine descends within the geologic formation, trapping the CO_2-enriched brine due to gravity segregation. This mechanism contributes to the reduction of CO_2 migration and enhances the storage capacity of the reservoir.

tNavigator models the solubility of CO_2 and other components using Henry's Law, the general form of which uses the following formula:

(Eq. 1) $$f = x * H$$

Where:

f = the fugacity of the component

x = composition of the component in the aqueous phase

H = Henry's Law constant

The Henry's Law constant for a specific component (e.g., CO_2) can be calculated as a function of pressure, temperature, and salinity in tNavigator using correlations developed by Li and Nghiem (Li & Nghiem, 1986). The latter correlation was chosen for its improved accuracy at modeling CO_2 and hydrocarbon gas solubility in high-salinity brines.

2.3.4 Mineral Trapping

Mineral trapping or *geochemical* trapping is another form of chemical trapping that occurs due to reactions between CO_2 and the geochemistry of the formation. During CO_2 injection into the reservoir, four primary drivers interact with one another: (1) CO_2 in the supercritical phase, (2) in situ hydrochemistry of the connate brine, (3) aqueous CO_2, and (4) the geochemistry of the formation rock. The interaction of these components results in CO_2 often being precipitated out as a new mineral. This new mineral is typically Ca-CO_3, or calcium carbonate (i.e., limestone).

Mineral trapping can also occur due to the adsorption of CO_2 onto clay minerals. Once hysteresis and solubility trapping are included in the model, geochemical formulae can be added through an internal geochemistry database to describe mineral-trapping reactions. For aqueous reactions, the following formulae were used:

$$CO_2(aq) + H_2O = H^+ + HCO_3^-$$
$$CO_3^{-2} + H^+ = HCO_3^-$$
$$OH^- + H^+ = H_2O$$

These three reactions are common ionic reactions that can occur in the reservoir between water and CO_2. The following formulas show the mineral reactions used in the model. Each mineral is commonly found within sandstone in an underground aquifer and causes the precipitation of carbon oxides in a solid state:

$$Anthorite\ (CaAl_2Si_2O_8) + 8H^+ = 4H_2O + Ca^{2+} + 2Al^{2+}$$
$$Calcite\ (CaCO_3) + H^+ = Ca^{2+} + HCO_3^-$$
$$Kaolinite\ (Al_2Si_2O_5(OH_4)) + 6H^+ = 5H_2O + 2Al^{3+} + 2SiO$$

While geochemical trapping can have a greater impact on CO_2 over hundreds or thousands of years, the short-term effects of these trapping mechanisms are small, and fluid movement is dominated by structural, residual and solubility trapping. Due to the extraordinarily long timeframes geochemical reactions take to see any applicable effect, the geochemical trapping mechanism is not assumed in the current model. As more data is received on the reservoir's geochemical properties, sensitivities could be run to determine the applicability of these traps.

2.3.5 Trapping Summary

Following the cessation of injection (in Year 2045), the mobile CO_2 experiences a rapid reduction as supercritical-phase CO_2 migrates through the pore space and becomes entrapped. Throughout the project's life span, residual trapping of supercritical CO_2 emerges as the predominant one among the various trapping mechanisms. Approximately 62% of the injected fluid undergoes secure sequestration through residual trapping within the pore space. The solubility of CO_2 into the connate brine facilitates the safe storage of around 13% of the injected CO_2. The remaining 25% of the injectate is subject to structural and hydrodynamic trapping. Figure 2-4 provides a breakdown of each trapping mechanism during the life of the project.

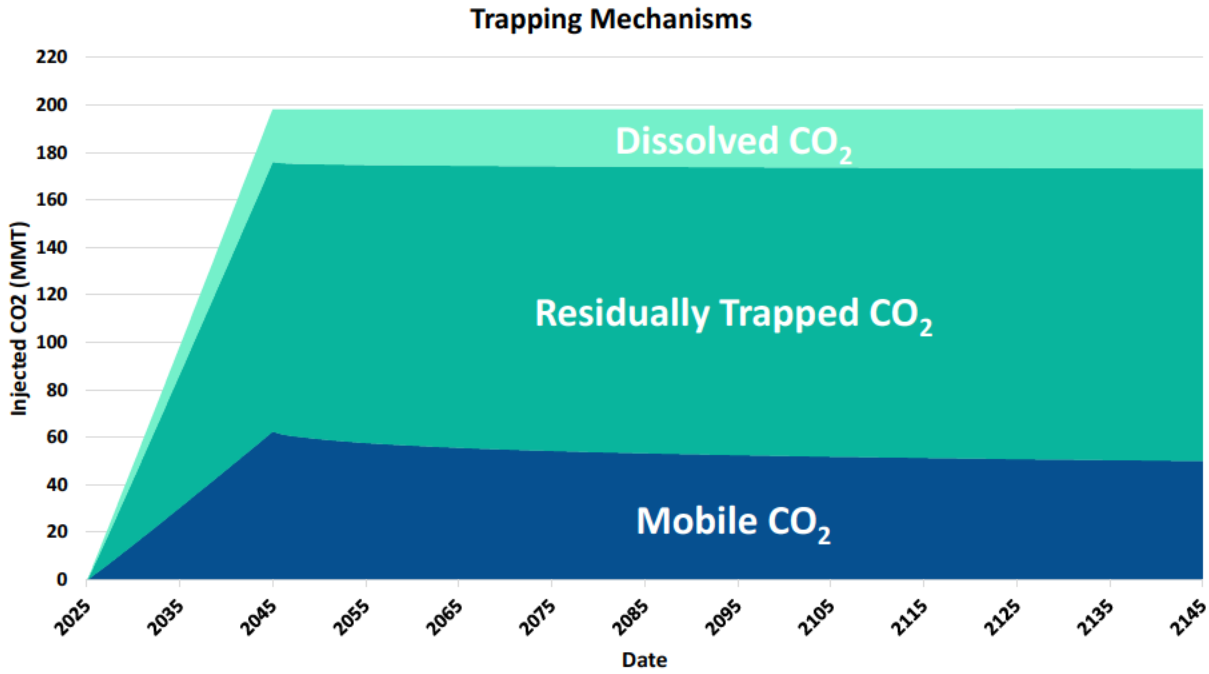

Figure 2-4 – Trapping Mechanisms Summary

2.4 Site Characterization Model

2.4.1 Static (Geocellular) Model Development

This section presents the geocellular model of the High West CCS Project, conducted to fulfill the requirement of SWO 29-N-6 **§3615.B.3.a**, which states that the AOR must be delineated using "computational modeling."

The geocellular 3D model and referred to as the Static Earth Model (SEM) (delineated in Figure 2-5), spans 15 mi x 15 mi laterally and is approximately 9,300 feet (ft) in average thickness. The SEM covers the entire Upper and Middle Miocene formations, including the sealing upper and lower confining zones (the UCZ and LCZ respectively). This model was constructed using Petrel software.

Figure 2-5 – Lower model surface utilizing the FS 8 horizon and depicting the fault intersections in the surface. The outline of the 3D seismic data used in the construction of the model is shown with a white polygon.

The 3D model was created in NAD27_LS1702 coordinate system and included a structural interpretation based on 79 wells. Of those wells, 64 were drilled inside the model boundaries with position data, well logs, 3D seismic data, faults and horizon from seismic interpretations in time, and public regional shape files. A list of these wells is provided in *Appendix B-10*. Of the 79 wells, 55 were used for the petrophysical evaluation. The flowchart in Figure 2-6 describes the process followed during the geocellular model construction.

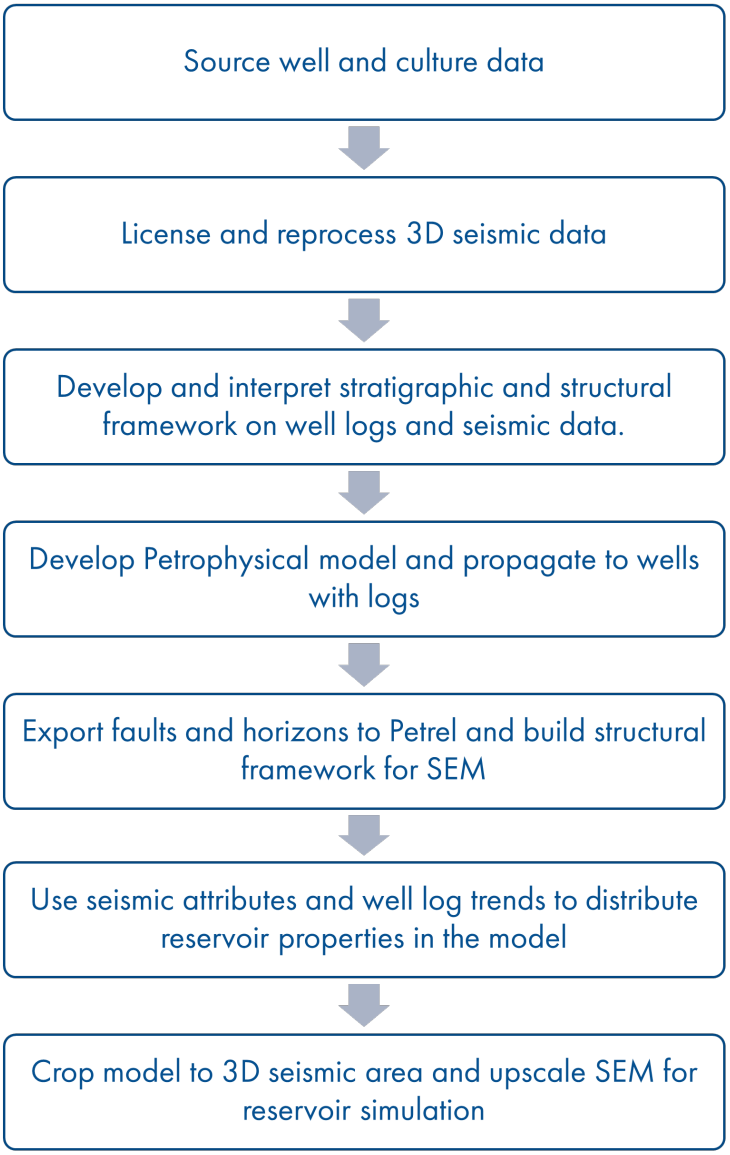

Figure 2-6 – Geocellular Model Workflow

2.4.2 Structural Framework

The 3D seismic interpretation of 23 faults and 34 surfaces of the stratigraphic framework were used to construct the 3D structural model for the High West CCS Project (Figure 2-7). The stratigraphic framework used in the High West CCS Project covers the Upper and Middle Miocene intervals. Two faults, both related to salt domes south of the project, extend upwards through the shallowest portions of the model while the remaining 21 faults mapped have either no offset at the base of the mapped framework or minimal offset within the High West CCS Project lease area.

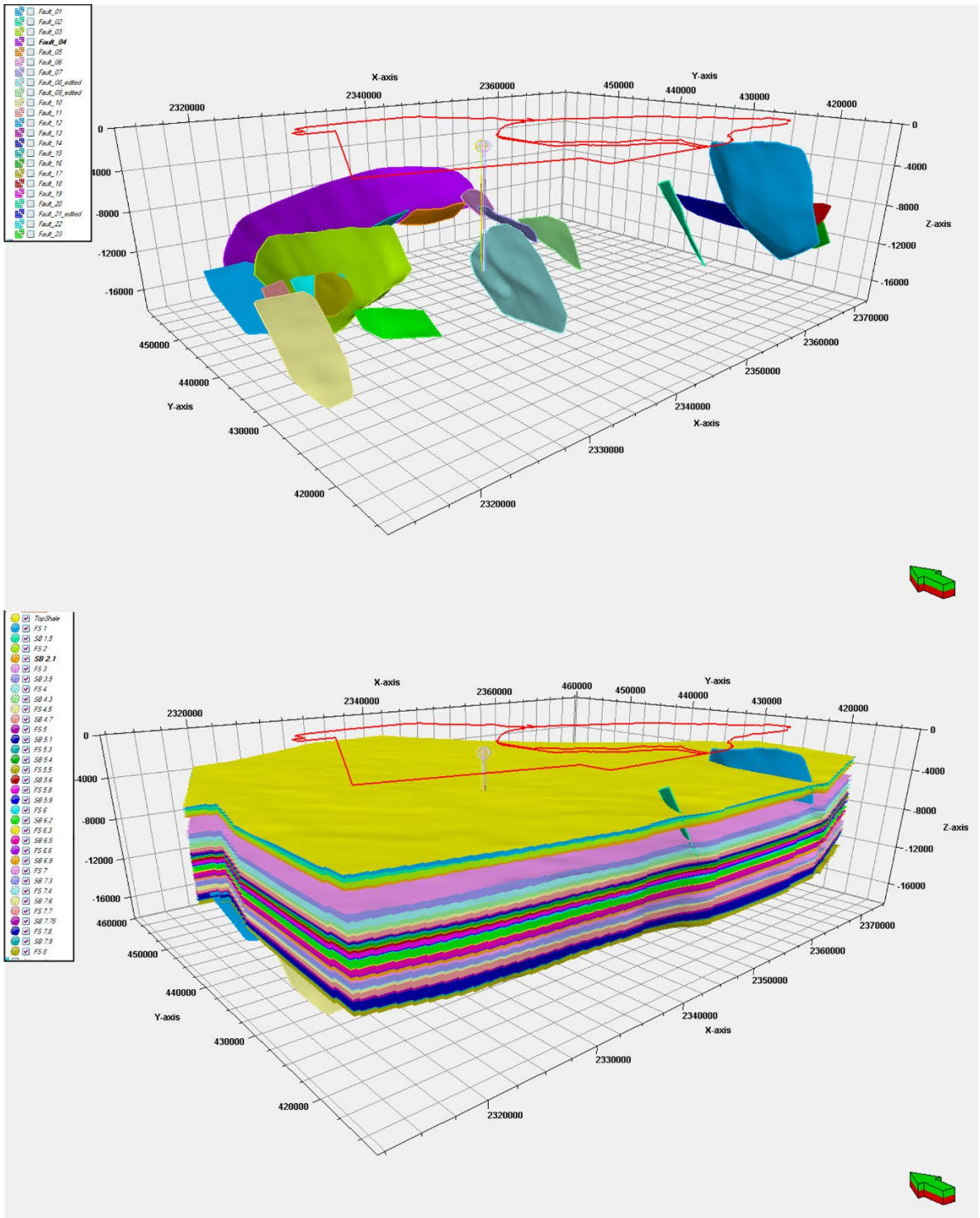

Figure 2-7 – Structural model faults and surfaces used in construction of the SEM displayed in a 3D view. The High West CCS Project lease area is shown with the red polygon displayed at sea level. All units are in feet.

Appendix B-1 and B-3 illustrate the faults for the top of the upper and lower confining surfaces, the UCZ (SB 2.1-SB 2.1B) and LCZ (SB 7.3-FS7.4), respectively. The majority of the faults mapped in the High West CCS Project area are related to older depositional features such as growth faults and salt-withdrawal basins present below the LCZ. Nine seismic time horizons and their corresponding well markers were used to develop a velocity model that was used to convert time horizons to depth. The velocity model was then used to generate 21 depth horizons that were used to populate the SEM and generate the 34 surfaces in the SEM. In total, 45 formation and biostratagraphic tops were used to further refine the model vertically.

The injection zone at the High West CCS Project, and the confining zones, were deposited in a deltaic to fluvial environment during the middle and upper Miocene. Sediments were deposited on a stable shelf with cyclicity between sand and shale provided by rising and lowering sea level as well as meandering channels that were bringing sediments to deeper water further south. The deepest sands in the injection intervals have characteristics of prograding deltaic sands that are coarsening upwards while the shallow sand at the top of the injection zone, and those above the injection zone, display characteristics of north-south oriented distributary channels that feed sediments to the south. Most of the injection intervals exhibit prograding to aggregating sand bodies that are oriented along strike to the paleo-shoreline. These depositional characteristics were captured in the interpretation of the seismic data and used in our SEM modeling to guide facies and reservoir properties distribution. Examples of these seismic interpretations are shown in Figure 2-8.

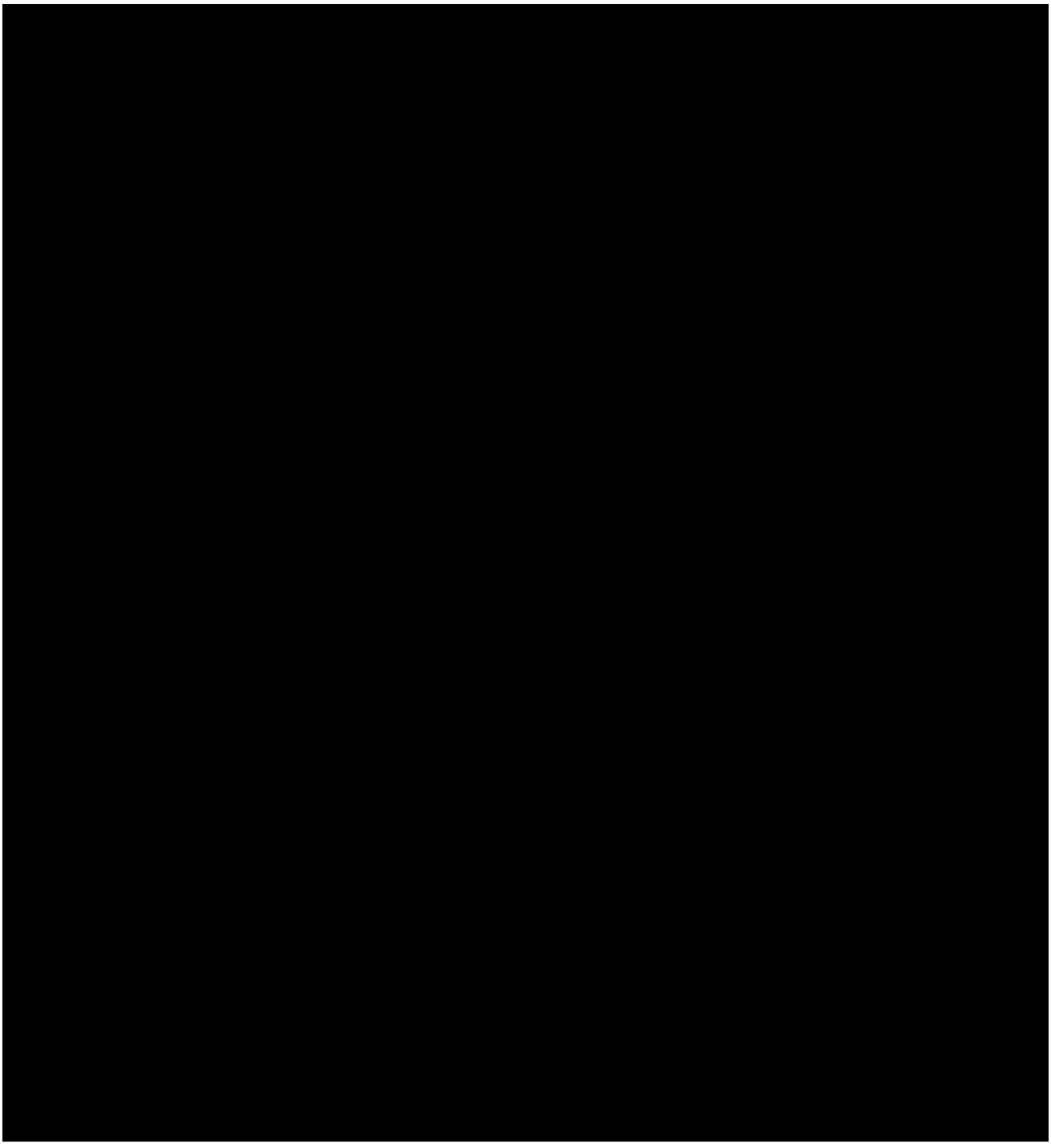

Figure 2-8 – Examples of seismic attribute maps guiding the population of reservoir properties into portions of the model away from well control. Yellows and red colors indicate sand-prone seismic signatures while browns represent shale-prone seismic signatures. The stars show the location of the type well on the individual maps for reference.

The mapped seismic attributes were used in the SEM to guide the continuity of the data in the major and minor directions while matching the well data. The petrophysical properties were distributed (e.g., facies and porosity) from 55 wells with available information, using the geostatistical modeling tools to preserve the heterogeneity and trends of the Miocene Formation. The anisotropy used in the lower Miocene units had one of two azimuths, in general, either an azimuth of roughly 160°, or 60°. This anisotropy corresponds with observed depositional trends described in the technical paper of Miocene-age sediments along the Gulf Coast (Snedden and Galloway, 2019). The two major trends seen in the geologic model are shown in Figure 2-9, with the 160 degrees NW-SE trend representing the fluvial facies and the 60 degrees NE-SW trend representing the paleo-shoreline-parallel deltaic facies.

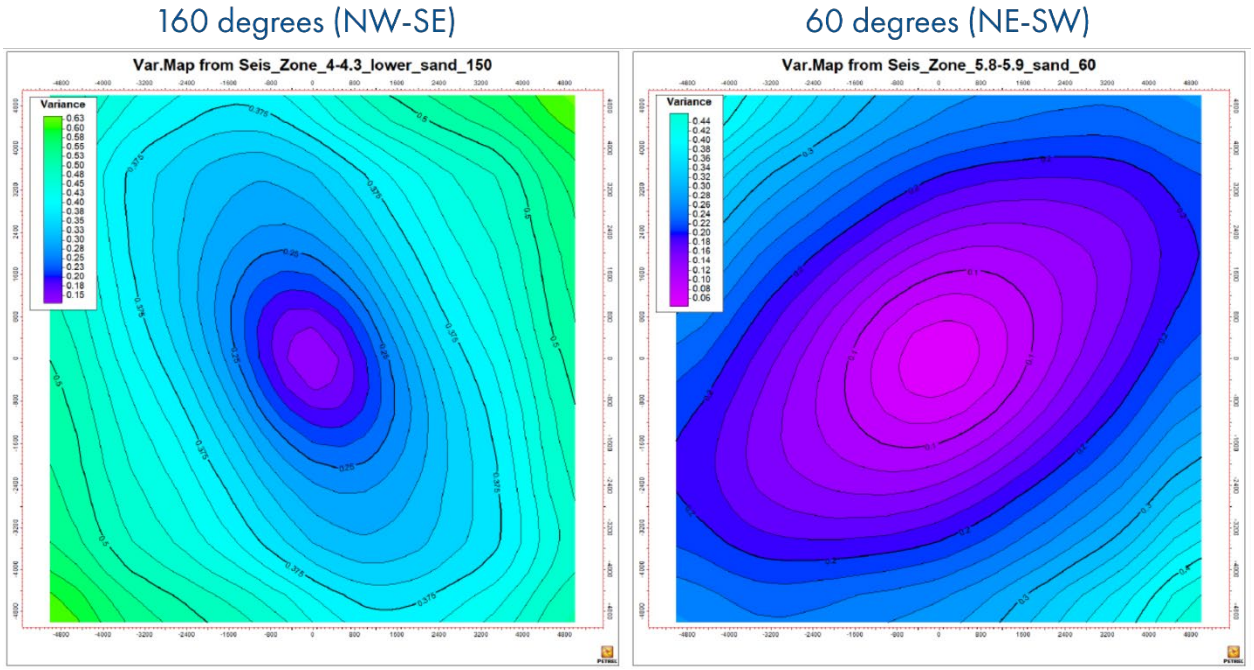

Figure 2-9 – Variogram trends from two layers demonstrating the two major trends seen in the data going into the SEM.

An example of well log data is displayed in Figure 2-10, with V_{clay}, SP, resistivity, lithofacies, effective porosity, and permeability from petrophysical interpretation, and the same properties displayed to the left in the 5.6-ft vertical average grid after modeling. The initial model was cropped to the seismic area and then upscaled. Table 2-1 details the initial geocellular model, which has 33 zones defined between 34 tops, including the entire Upper and Middle Miocene Formation as well as the UCZ (SB 2.1 to SB 2.1B) and LCZ (SB 7.3 to FS 7.4) shales.

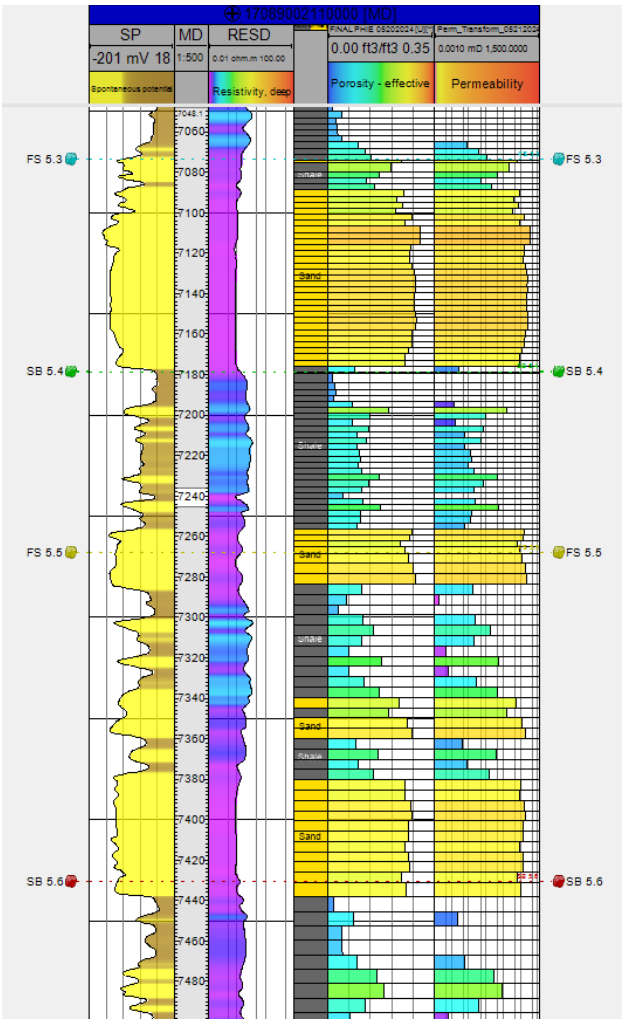

Figure 2-10 – Example Well Log (Waterford Oil Company No. 001) with Petrophysical Log Data from the SEM. Facies, effective porosity and permeability from the SEM at the well location are shown in the right three tracks.

Table 2-1 – Geocellular Model Construction

Regional SEM	
Mapping area	15 mi x 15 mi
Grid block dimensions	200 ft x 200 ft
Grid dimensions (cell count, I-J-K)	396 x 396 x 1667
Vertical dimension average	5.6 ft
Upscaled SEM	
Grid block dimensions	250 ft x 250 ft
Grid dimensions (cell count, I-J-K)	247 x 184 x 292
Vertical dimension average	30 ft
Vertical dimension average - injection zone	18 ft
Model Inputs	
No. of faults	23
No. of surfaces	34
No. of wells	59
Model properties	Facies, $Ø_{effective}$, permeability

2.4.3 Petrophysical Modeling

Petrophysical data was analyzed for 55 wells and 33 zones using geostatistics. These analyses included the use of general statistical information, histograms, and variograms (vertical, major, and minor directions). The petrophysical data analyzed were facies, effective porosity ($Ø_{Effective}$), and permeability. Log properties were upscaled to the grid at the intersection of the well and the SEM grid. The upscaled log properties were used for estimation of the properties at the remaining grid cells away from the wells.

2.4.3.1 Facies

Figure 2-11 shows the general statistics for the facies property from the entire model. A two-facies model was chosen due to the age of the well log data, the lack of information to generate a finer subdivision between sand and shale, and the lack of calibration data. The number of facies used will be reassessed once the stratigraphic test well data is collected and analyzed.

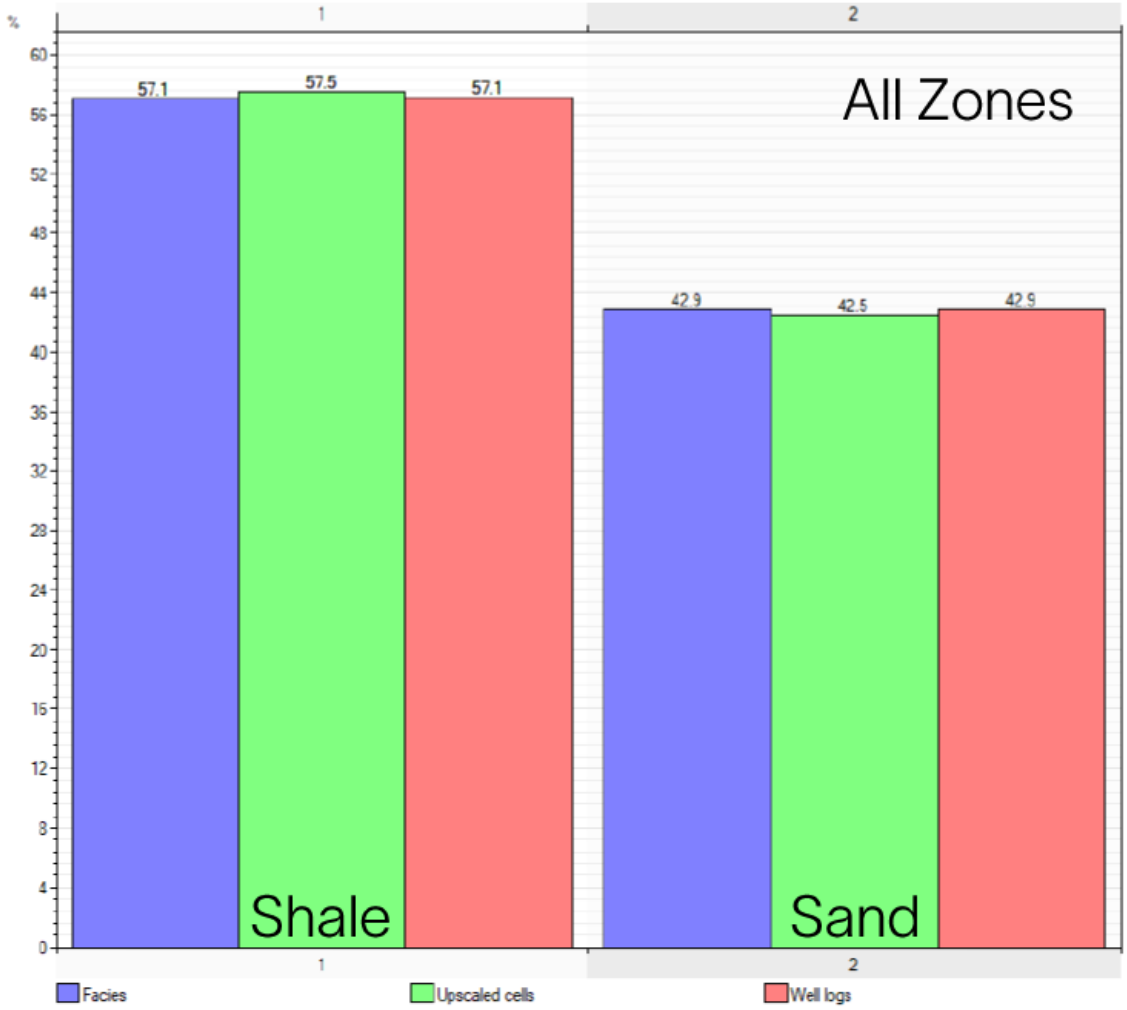

Figure 2-11 – General statistics for the entire model for the facies property. Each zone was also checked individually. Raw data is shown in red, upscaled cells in green, and populated property in purple.

The primary differentiator between the sand and shale facies was the V_{clay} percentage. V_{clay} greater than 35% was considered shale while 35% and lower was considered sand. For every SEM zone, vertical proportion curves were calculated, variogram ranges were estimated, seismic attribute maps by zone were used to estimate facies trends, and then a facies was estimated by zone at every grid cell via Sequential Indicator Simulation (SIS). Figure 2-12 shows a vertical section displaying the facies property extracted from the SEM along a west-east profile.

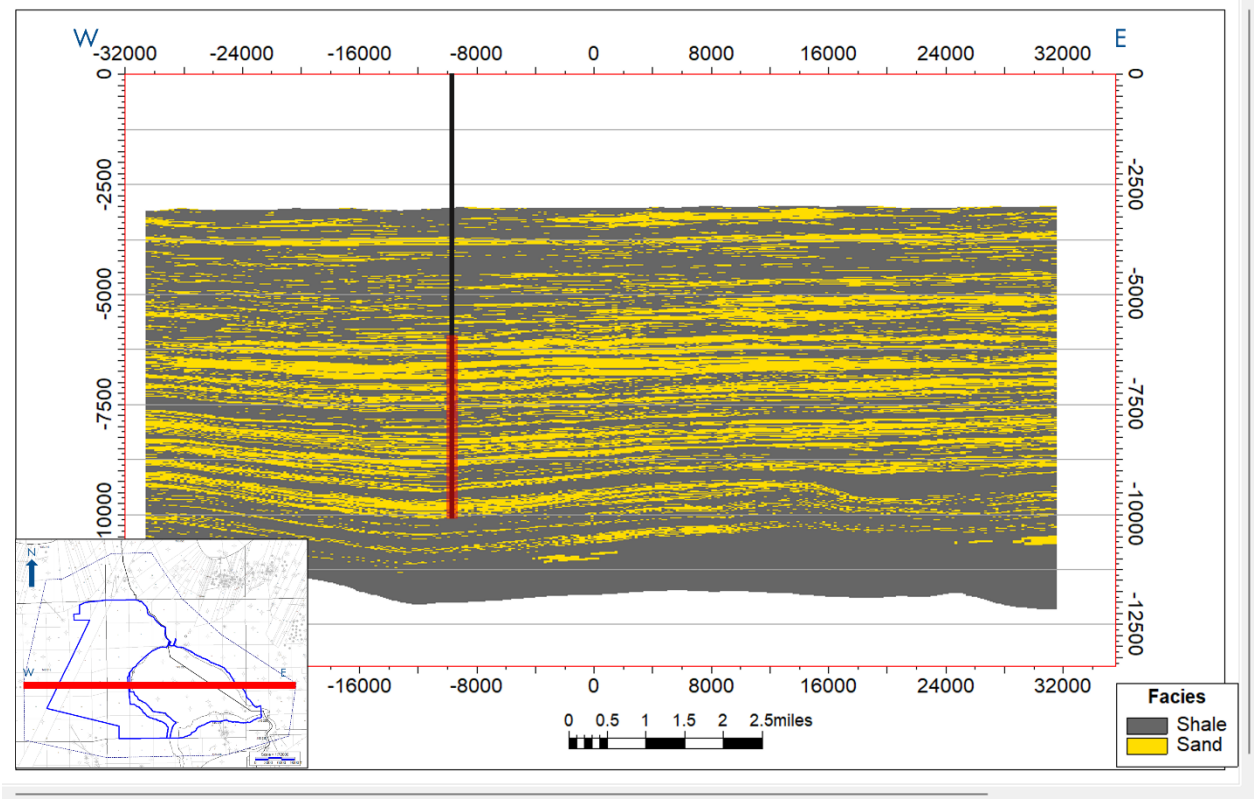

Figure 2-12 – Facies property extracted from the SEM along a west-east profile. Yellow represents sand facies and gray represents shale. The injection site is marked with a vertical black line as a well and the injection zone is highlighted with the vertical red bar along the well.

2.4.3.2 Effective Porosity ($Ø_{Effective}$)

$Ø_{Effective}$ is the reservoir property that controls the amount of CO_2 storage in the reservoir as well as being correlated to permeability. Facies is the main driver for the likelihood of a portion of the reservoir to have higher $Ø_{Effective}$. Figure 2-13 shows a histogram display of the $Ø_{Effective}$ property for the entire model, split by facies, comparing the raw data (from logs in red) to the upscaled logs (in green) and populated grid property (in purple). The sand facies, which acts as the reservoir, has a much higher average $Ø_{Effective}$ property than does the shale facies that forms the seals.

$Ø_{Effective}$ is calculated zone by zone, conditioned to facies, using separate variograms by zone and by facies. The property is distributed via Gaussian Random Function Simulation (GRFS). Figure 2-14 shows the same west-east vertical section from the SEM as Figure 2-12 but displaying the $Ø_{Effective}$ property.

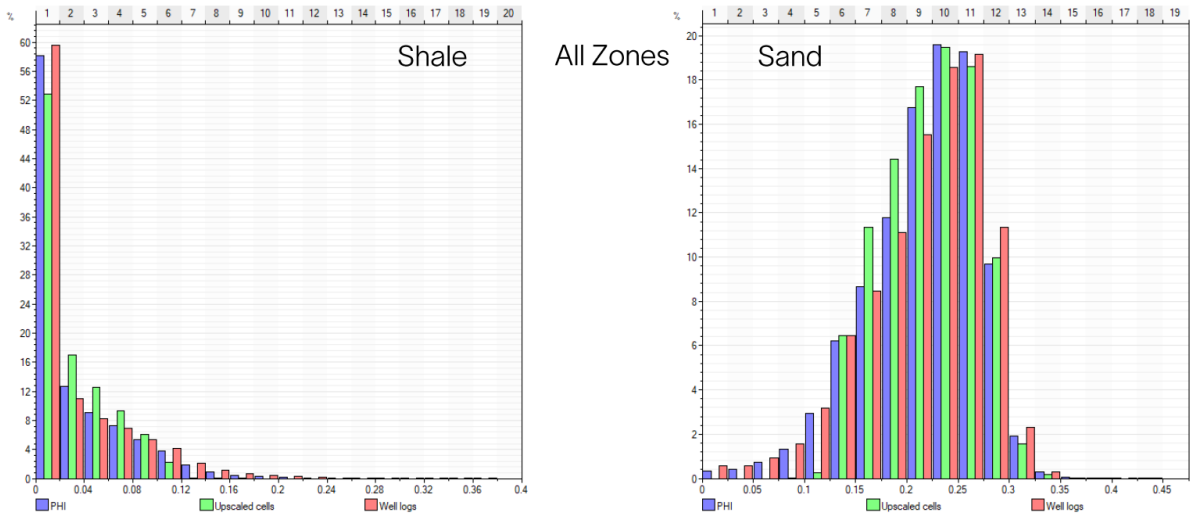

Figure 2-13 – Histogram display for all zones. Raw data is shown in red, upscaled cells in green, and populated property in purple. Typical values of $Ø_{Effective}$ range from 0-2% in shales and 23-28% in sands.

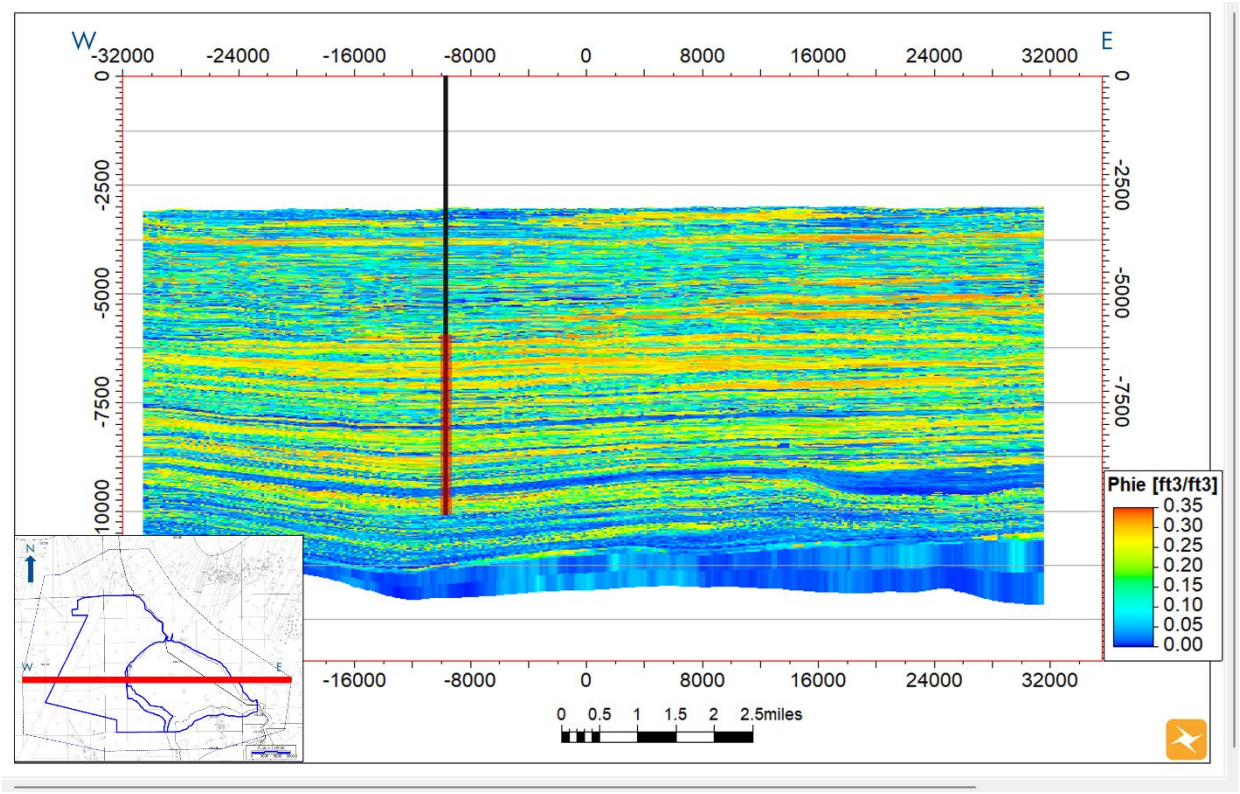

Figure 2-14 – $Ø_{Effective}$ property extracted from the SEM along a west-east profile. Yellow and orange colors represent high porosity rock, typically sand, and cooler blue colors represents low porosity rock, typically shale. The injection site is marked with a vertical black line for a well and the injection zone is highlighted with the vertical red bar along the well.

2.4.3.3 Permeability

Permeability is typically measured in core samples and then related back to well log calculations based on the depth of the core samples. Permeability can be estimated by nuclear magnetic resonance well logs or by injection or production tests. Since none of these data are currently available locally in the High West CCS Project, data was used from privately accessed core databases, filtered to samples from similar depths, pressures, and depositional environments, to relate $Ø_{Effective}$ to permeability at the High West CCS Project. Figure 2-15 shows the same west-east vertical section from the SEM, as the previous figures, displaying the permeability property. The transform used calculated permeability from the $Ø_{Effective}$ property is shown in Figure 2-16.

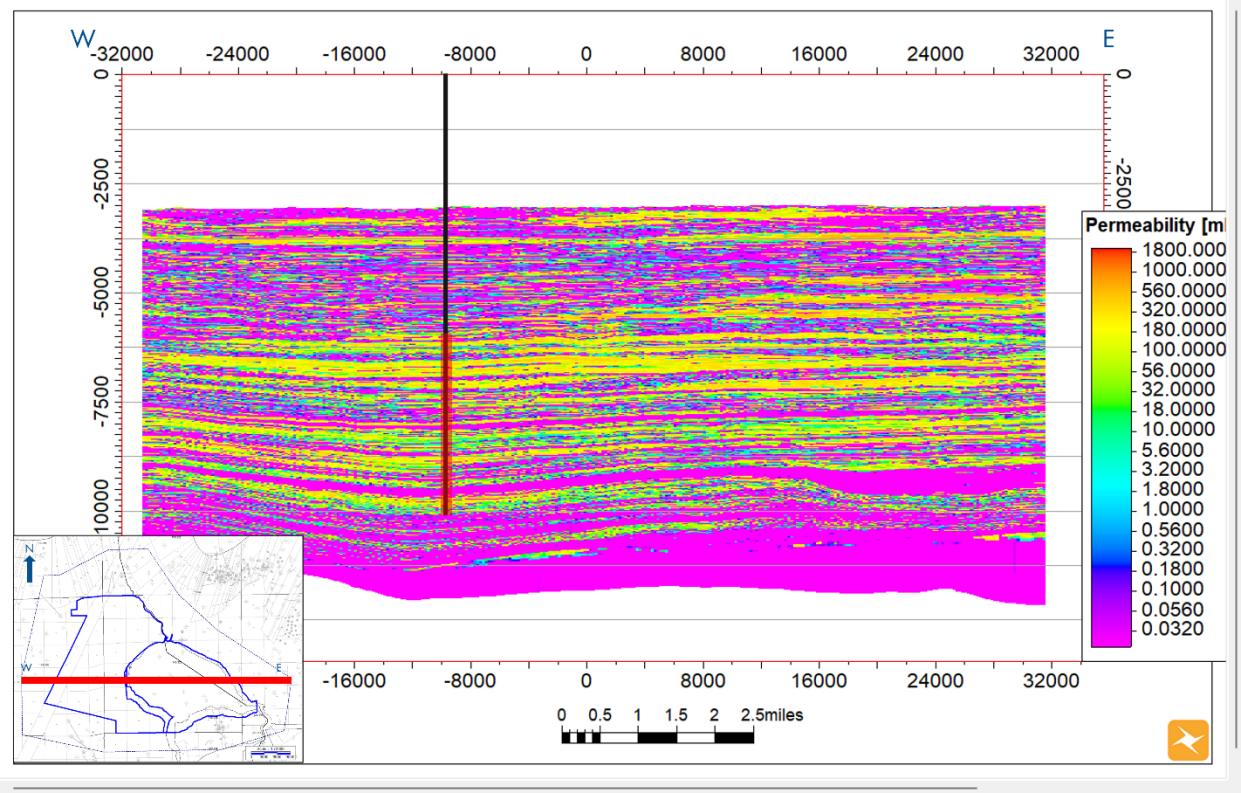

Figure 2-15 – Permeability property extracted from the SEM along a west-east profile. Yellow and orange colors represent high permeability rock, typically high porosity sand, and cooler blue and purple colors represents low permeability rock, typically shale. The injection site is marked with a vertical black line for a well and the injection zone highlighted with the vertical red bar along the well.

Figure 2-16 – Porosity-permeability transform developed from privately accessed core databases using samples collected from rocks deposited in similar depths, pressures and depositional environments. The points on the cross plot represent the core sample measurements of porosity and permeability while the curved line fitted through the data points represents the transform used to calculate permeability from the SEM porosity values. The displayed equation is the calculated permeability transform used.

Figure 2-17 is a display of the three attributes modeled over the five injection zones (FS 4 to SB 7.3). The structural and facies 3D models were used for the fault slip potential (FSP) analysis in the modeled area.

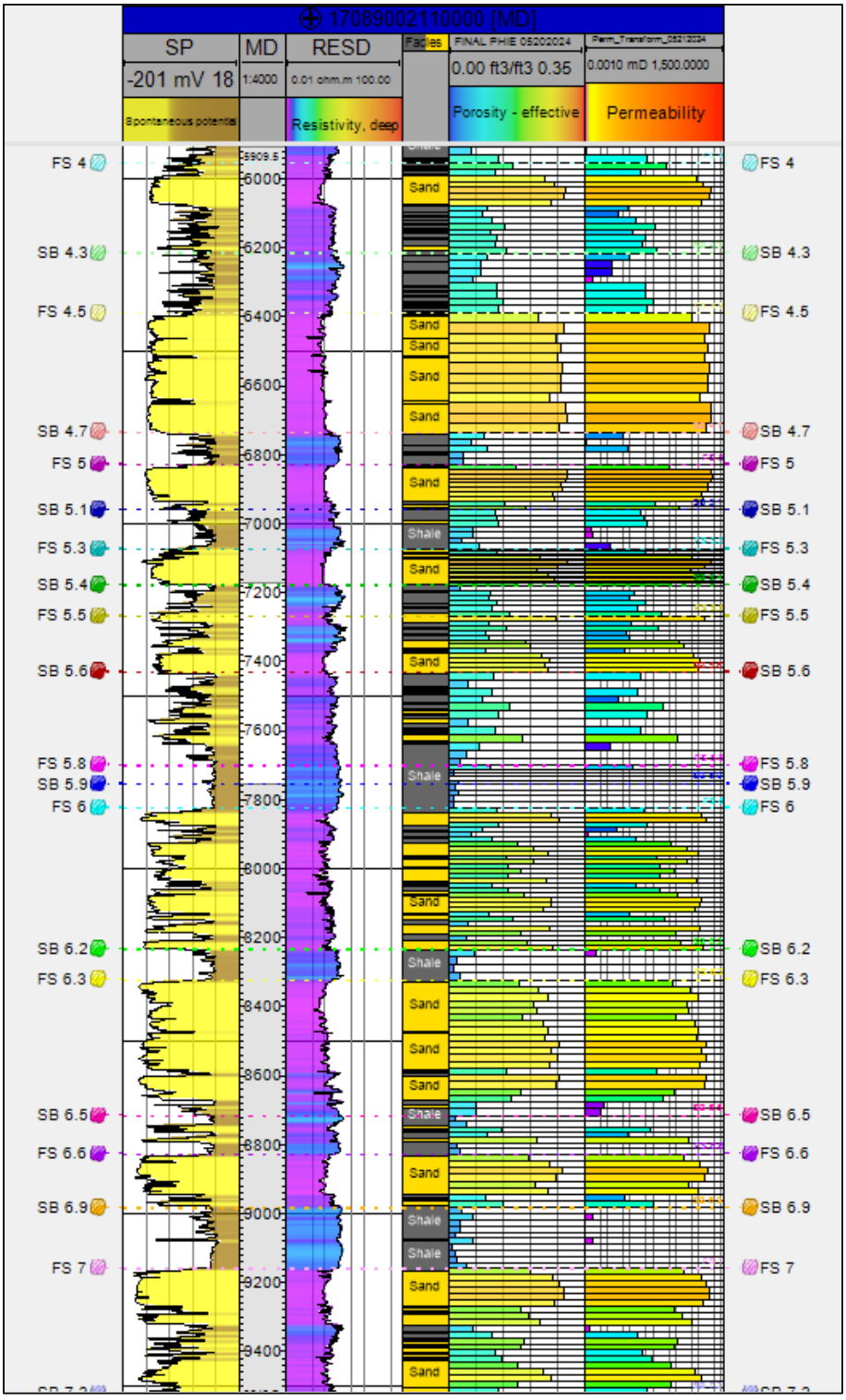

Figure 2-17 – Modeled injection zone (FS 4 to SB 7.3): Facies, $Ø_{Effective}$, and Permeability compared to the Waterford Oil Company No. 001 well logs used to populate the properties.

2.4.4 Upscaling the SEM for Reservoir Simulation.

The initial SEM built for the High West CCS Project had an average cell thickness of 5.6 ft and contained over 260 million grid cells. The initial SEM was upscaled for computational efficiency by merging grid cells with 0-5 ft of thickness and to vertically coarsen the non-reservoir intervals outside the injection zone while preserving the vertical anisotropy in porosity and permeability. In the coarsened grid cells, porosities were averaged, dominant facies were assigned and permeabilities were recalculated using the Miocene Core Study porosity-permeability transform. Examples of the upscaled SEM and porosity and permeability properties are shown in Figure 2-18.

A third facies was created after upscaling from the Petrel model. Due to the nature of upscaling, some cells were dominantly shale but averaged to be moderate porosity and permeability. To better reflect that these grid cells would be more akin to sandy shales or shaley sands, a third facies was implemented from the "sandy shales". A cutoff of 5 millidarcy (mD) was used to separate the sandy shales from the shale facies. This added facies cutoff only affects 11% of the active grid cells in the model and does not significantly impact the results of the model. The inclusion of a third facies provides additional conservatism as it allows the CO_2 plume to migrate further.

The porosity values in the sands (Facies 3) had a pore volume (PV) weighted average of 23.64%. The porosity values in the shaley sands (Facies 2) had a PV weighted average of 22.38%. The porosity values in the shales (Facies 1) had a 9% PV weighted average.

The porosity-permeability relationship was then applied to the model, resulting in a PV weighted average of 118 mD for the sand facies. The sandy shale facies permeability had a PV weighted average of 67 mD. The shale facies permeability had a PV weighted average of 0.54 mD.

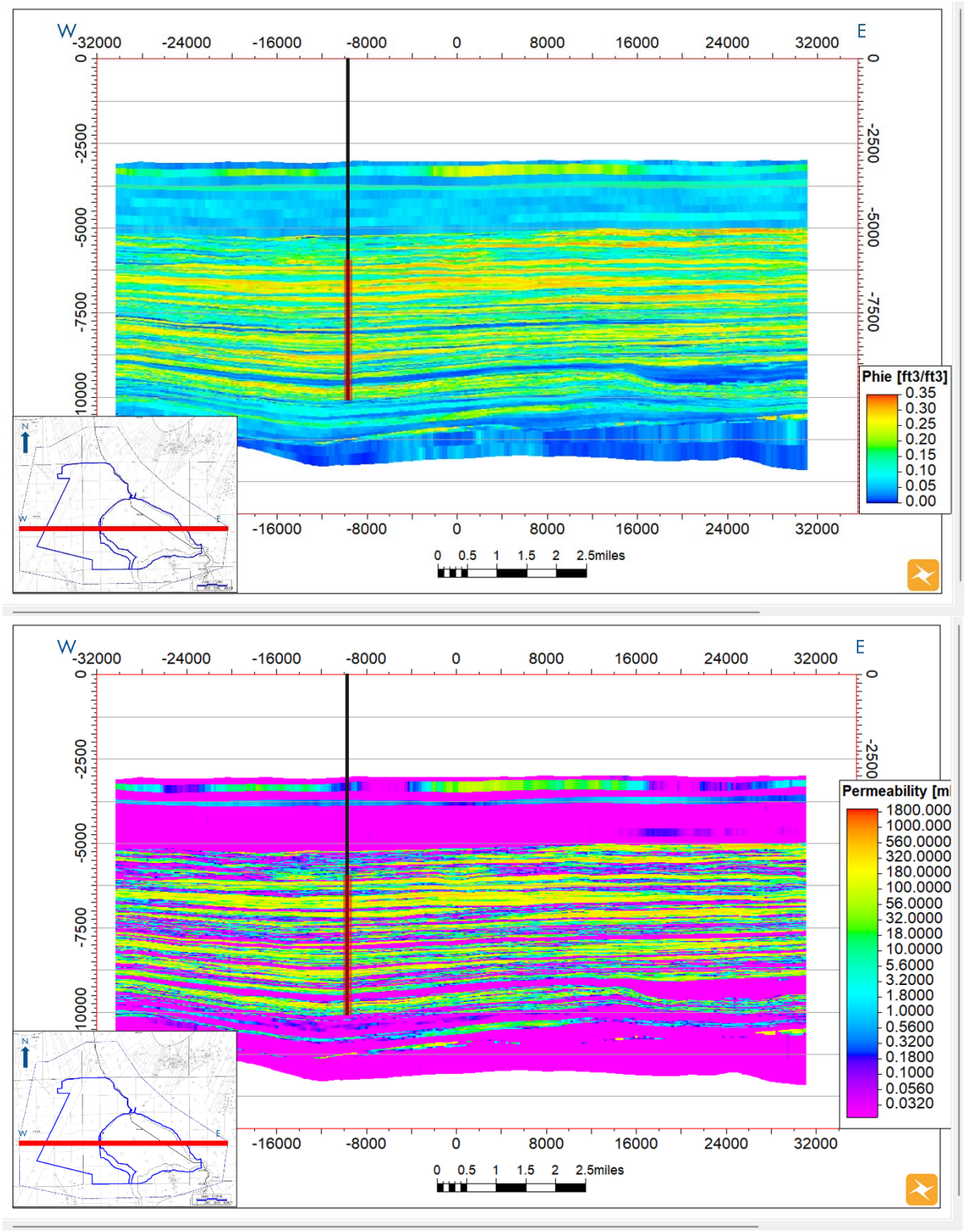

Figure 2-18 – Examples of the porosity (top) and permeability (bottom) properties along a west/east vertical profile from the upscaled SEM. Consolidating thin layers and coarsening of the non-injection intervals increased the efficiency of the simulation. The injection site is marked with a vertical black line and the injection zone is highlighted with the vertical red bar along the well.

The 3D structural grid with facies, $Ø_{Effective}$, and permeability properties distributed across every zone were exported as a RESQMLv2 file, to run the compositional dynamic simulation in tNavigator.

A table of the SEM zone values is provided in *Appendix B-11*.

2.5 Dynamic Plume Model

2.5.1 Model Orientation and Gridding Parameters

2.5.1.1 Spatial Conditions

As discussed earlier, tNavigator uses the Petrel geologic model as an input. The model was upscaled from its original grid cell dimensions to now be 250 ft x 250 ft x ~20 ft. To mitigate computational demands, the confining shales were split into fewer layers. The upper shale is split into nine layers (~225 ft on average) and the lower shale is split into two layers (~270 ft on average). The model uniformly covers an area of approximately 47,100 acres (~74 square miles (sq mi)). The grid extends 247 cells in the X-direction (east/west), 184 cells in the Y-direction (north/south), and 292 cells in the Z-direction. Figure 2-19 provides a visual representation of the total area covered by the grid in the project zone.

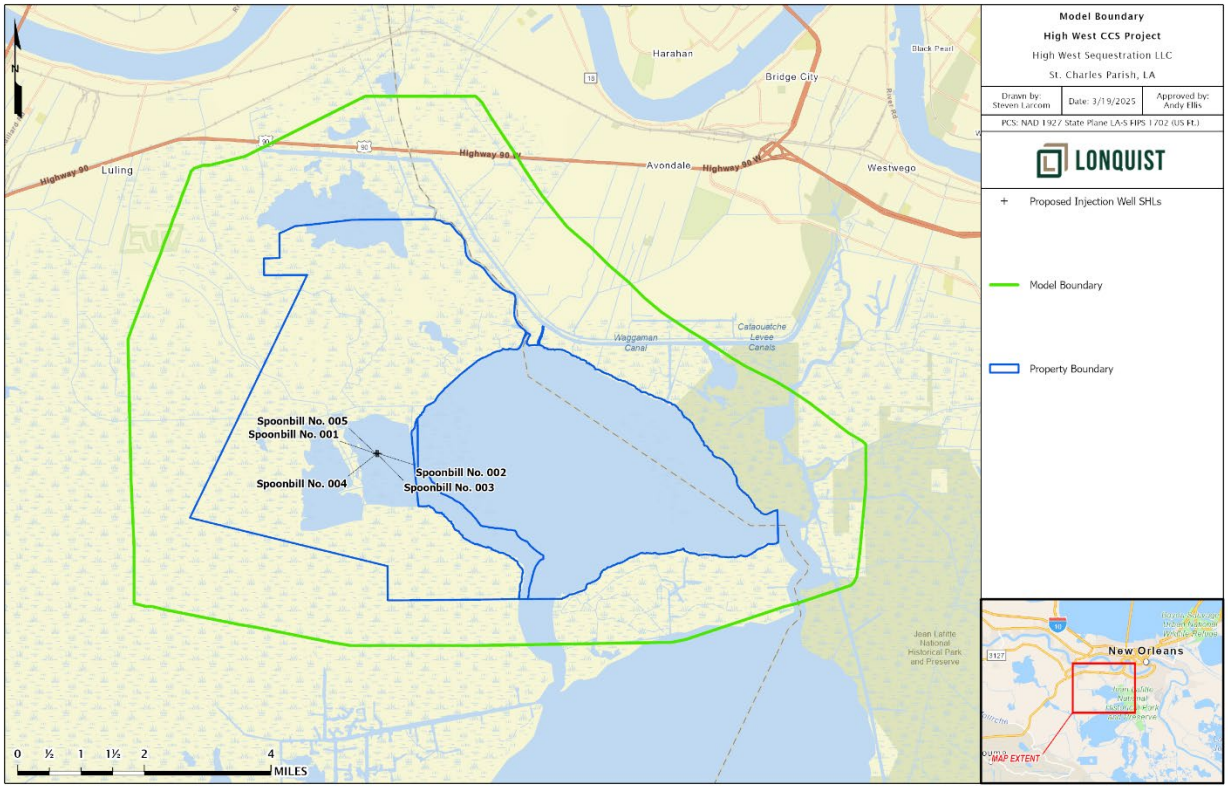

Figure 2-19 – Modeled Area

The model consists of approximately 13.3 million grid cells (~9.5 million active grid cells). To improve the computational efficiency of the model and accuracy of the results, a pore volume cutoff was applied to the grid. This cutoff was included to reduce the total amount of grid blocks and remove any cells that may cause numerical errors while preserving the major flow paths of the injected CO_2. A value 5,400 ft^3 was chosen as the pore volume cutoff which equates to less than 3% of the average pore volume per grid cell.

Multiple distinct sand packages have been identified as prospective candidates for supercritical CO_2 injection. Each package is stratigraphically confined by interbedded shales and shale baffles, serving as potential barriers to impede CO_2 migration. The integration of 3D seismic data has validated the geocellular model, offering a more precise depiction of the sand packages within regions characterized by substantial gaps in well data. Following identification, these sand packages were targeted for CCS injection with five injectors.

2.5.1.2 Boundary Conditions

Boundary conditions were chosen based on geologic research into the depositional environment. The Gulf Coast sands within the project area display extensive interconnectivity across the region. To emulate this highly connected nature, an infinite-acting reservoir approach is utilized. This method enables the accurate simulation of the pressure response arising from supercritical CO_2 injection. Achieving this specific objective is realized through strategically positioning "volume modifiers" along the grid edges. A value of 10,000 is applied uniformly along the edge of the grid, as Figure 2-20 illustrates, to enable infinite-acting behavior in the dynamic model. The upper and lower confinements serve as sealing boundaries due to their very low permeability.

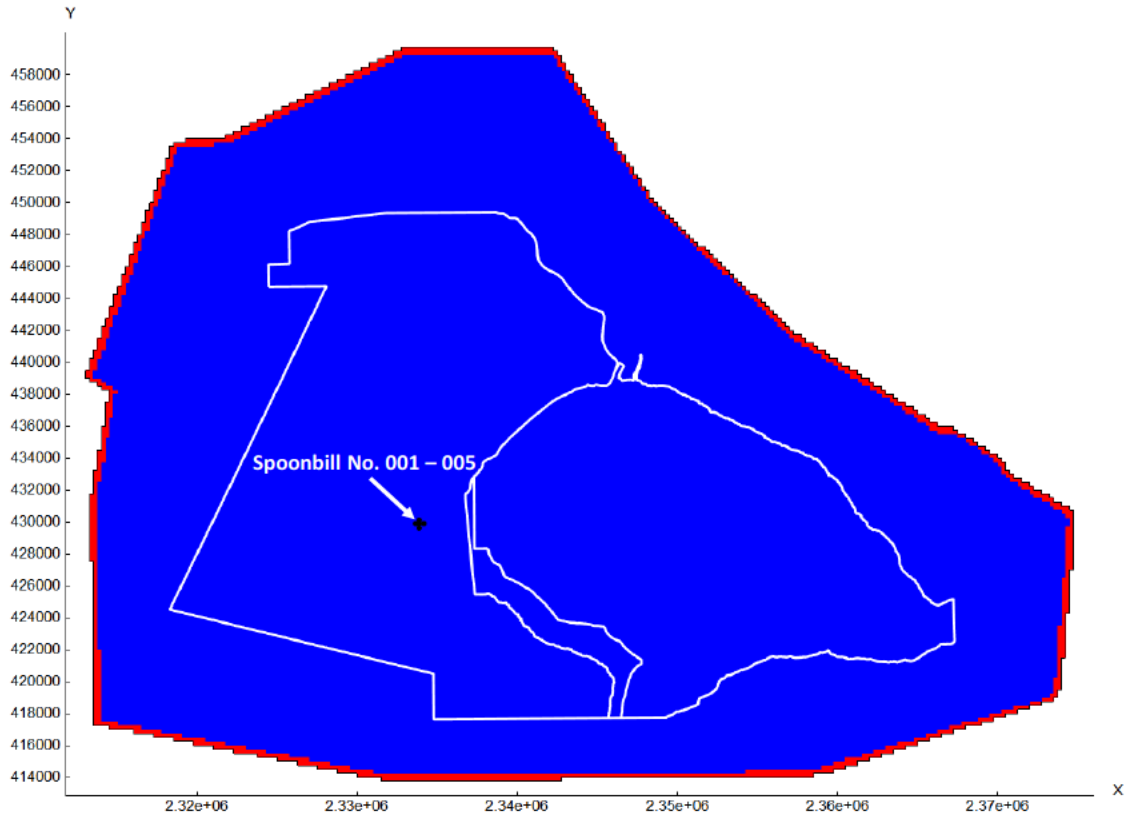

Figure 2-20 – Volume Modifiers as Applied to the Grid (the red line representing the 10,000 value)

The dynamic simulation model was initialized with transmissibility for all faults. Under this condition, the simulator will allow fluids to move between sand facies grid blocks that are juxtaposed against a fault face, according to the cross-sectional area through which these blocks are connected. In practical terms, fluid cannot flow across the fault between two grid blocks when one of those grid blocks contains permeable sand and the other contains impermeable shale. Under this approach, the faults will tend to seal against any and all flow. Since the faults are primarily below the injection intervals, there was no significant change in the areal extent of the CO_2 plume.

2.5.1.3 Model Time Frame

The model spans 120 years, comprising 20 years of active injection followed by 100 years of density drift. In this scenario, the model begins in Year 2025 and ends in Year 2145. This time frame is sufficient to capture the migration of the carbon plume until it achieves stabilization. The model results are further discussed in Section 2.7.

2.5.2 Initial Conditions

The dynamic model was built using the exported geocellular model and initialized with the following assumptions in Table 2-2. Porosity values were distributed using the GRFS method across the injectable sands and exported from Petrel, with values ranging from 0.01% to 33.27% in the injectable intervals. Offset core data and petrophysical analysis were utilized to establish

a permeability-porosity relationship, which was subsequently incorporated into the model. This integration yielded values within the range of 0.001 to 734 mD. An upscaled K_V/K_H ratio of 0.1 was also implemented into the model. The pore and fracture pressure gradients were calculated to be 0.465 pounds per square inch per foot (psi/ft) and 0.698 psi/ft, respectively. A regional and well-log review estimated the temperature gradient to be 0.98 Fahrenheit per 100 ft (°F/100 ft). Salinity was determined to be around 125,000 parts per million (ppm).

Table 2-2 – Initial Conditions Summary

Inputs	Values	Data Source
Pore Volume Weighted Average Porosity (%)	18.2	Dynamic Model Output
Pore Volume Weighted Average Permeability (mD)	69	Dynamic Model Output
Kv/Kh Ratio	0.1	See Section 2.5.2.1
Pore Pressure Gradient (psi/ft)	0.465	See Section 2.5.2.2
Fracture Pressure Gradient (psi/ft)	0.698	See Section 2.5.2.3
Mean Surface Temperature (°F)	72	See Section 2.5.2.4
Temperature Gradient (°F/100 ft)	0.98	Offset Well Review
Salinity (ppm)	125,000	See Section 2.5.2.4

2.5.2.1 Distribution of Porosity and Permeability

Petrel was utilized to distribute the porosity across the grid. As described in Section 2.4.3, the porosity was distributed using simple Gaussian methods. Distributing these values in such a fashion allowed the model to characterize the injection zone more accurately between large gaps in well data. Figures 2-21 and 2-22 highlight the porosity and permeability distributions throughout the dynamic simulation model, respectively.

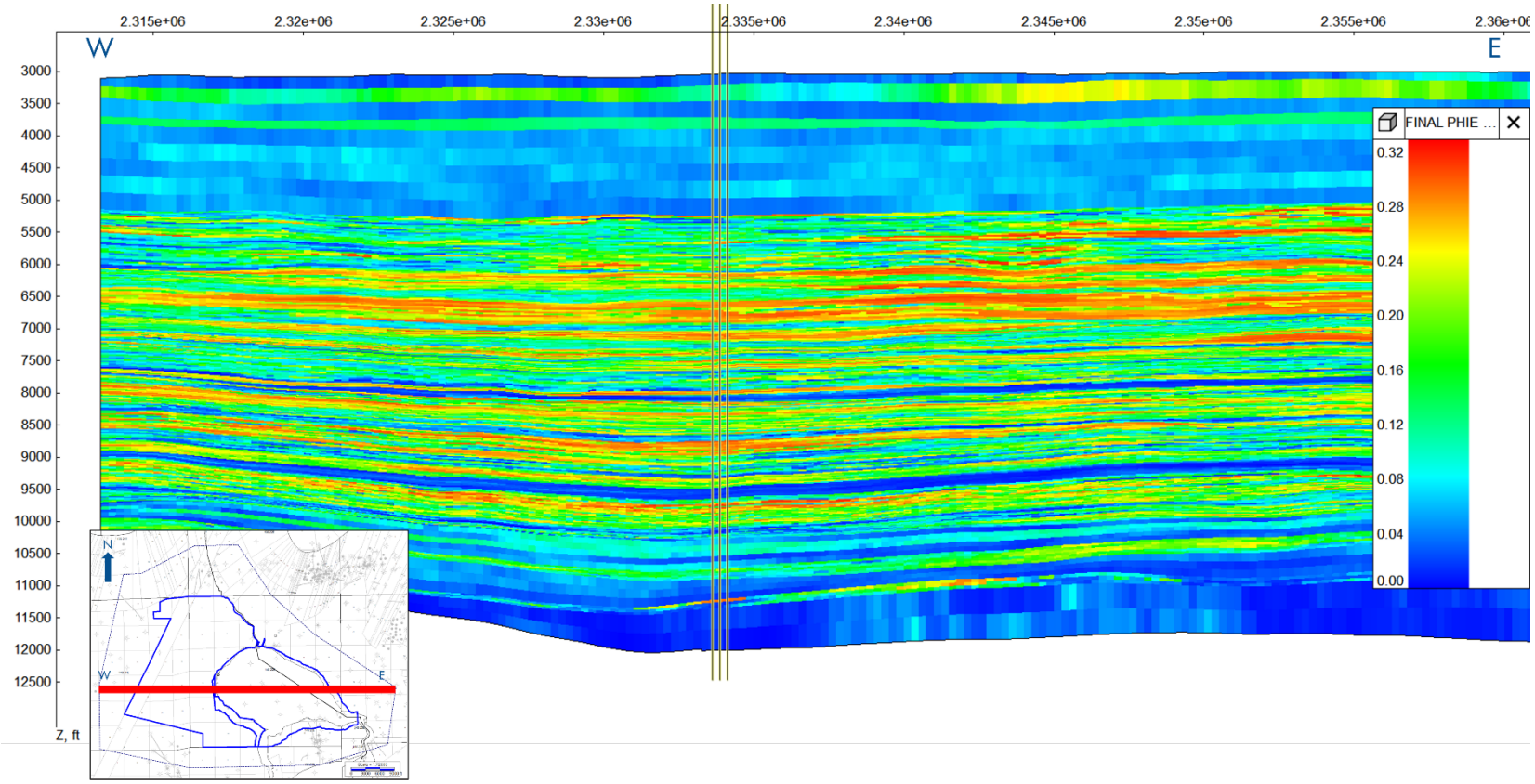

Figure 2-21 – Porosity (decimal fraction) Cross Section of the Dynamic Model

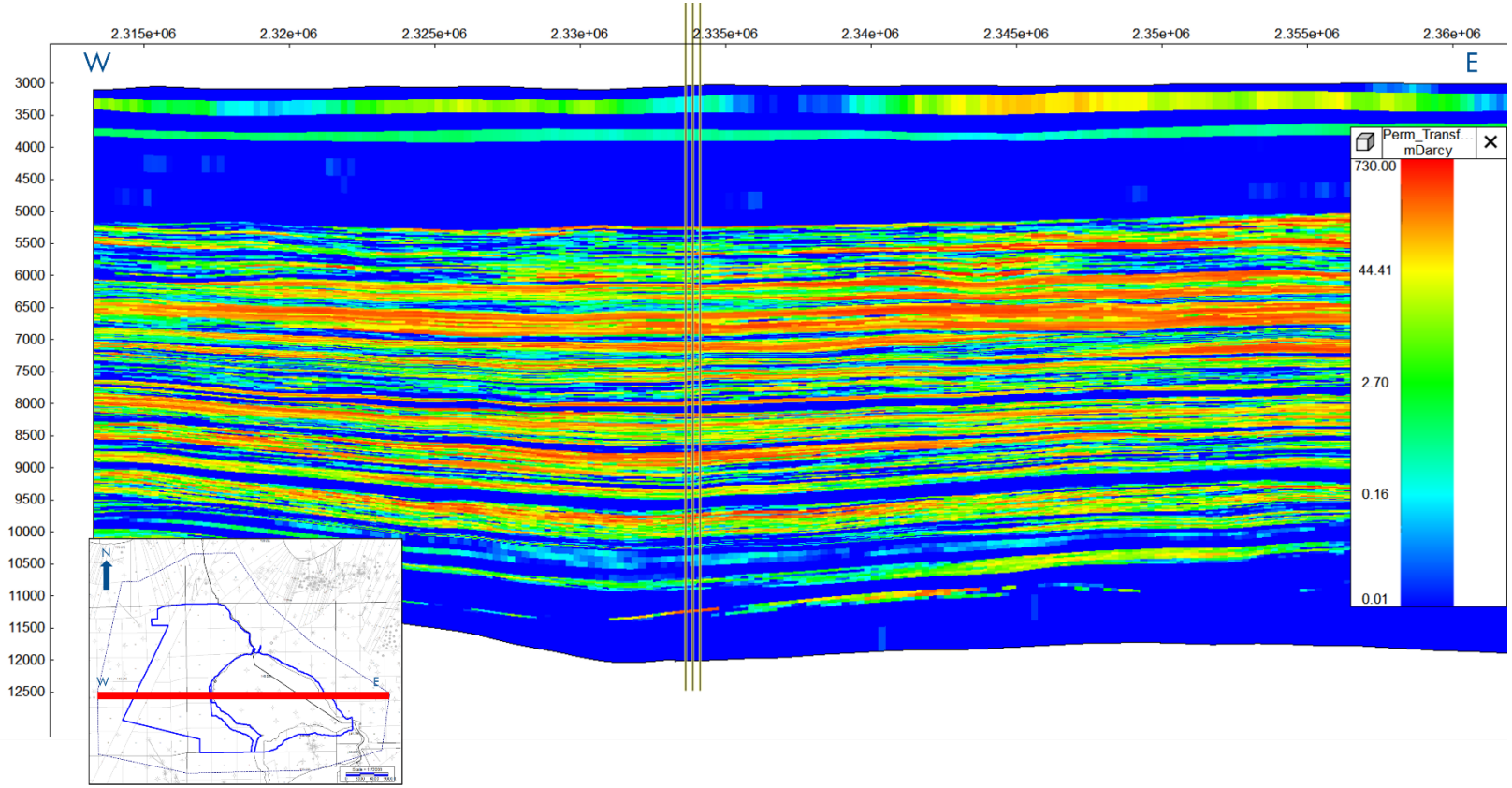

Figure 2-22 – Permeability (mD) Cross Section of the Dynamic Model

A K_V/K_H ratio of 0.1 was used to determine the vertical permeability in the model. A study conducted in the Frio sands, an analogous reservoir, suggests that K_V/K_H ratios from core data may have a wide range of values as seen in Figure 2-23 (Hovorka et al., 2003). Core data may indicate K_V/K_H ratios in the range of 0.9 to 1 at the core plug level. However, the choice of 0.1 as a value represents a standard upscaled value when extrapolating to the larger model grid-block scale, especially for intervals with high permeability. When looking at the scales smaller than the grid thickness (20 ft), there is a high likelihood of vertical permeability variations that would result in a lower K_V/K_H value.

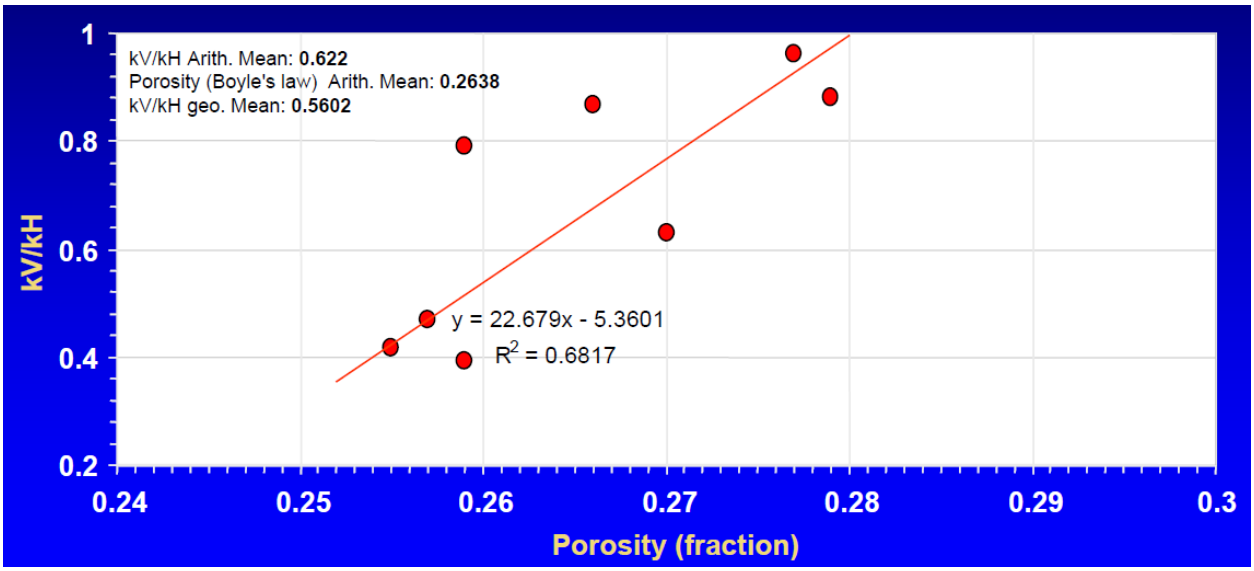

Figure 2-23 – K_V/K_H vs. Porosity Relationship (Hovorka et al., 2003)

For flow perpendicular to the bed boundaries (i.e., vertical flow), the flow will be dominated by the lowest permeability layers and reflected by a harmonic average of permeability data ("flow in series"). Conversely, the flow parallel to bed boundaries will be dominated by the highest permeability layers and reflected by an arithmetic average of permeability.

While perhaps appearing small relative to core data, a K_V/K_H ratio of 0.1 being a relatively high value is an important highlight. In a reservoir simulator, the flow between blocks is determined not by permeability but by the transmissibility between two adjacent blocks. The transmissibility between rectangular grid blocks is directly proportional to permeability multiplied by the cross-sectional area through which fluids pass, all divided by the distance separating the centers of the two grid blocks. This relationship can be expressed using the following equation:

(Eq. 2) $$T = k \times {}^{A}/_{L}$$

In this context, where A represents the cross-sectional area and L denotes the length of the flow path, there are distinct characteristics for vertical and horizontal flow between grid blocks. In vertical flow, the cross-sectional area (A) is considerably larger, while the length of the flow path (L) is relatively shorter. Conversely, in the case of horizontal flow between grid blocks, the area

(A) is much smaller, and the length (L) is significantly greater. In the context of this simulation model, given a K_V/K_H ratio of 0.1, the vertical transmissibility will be 312.5 times higher than the horizontal transmissibility.

2.5.2.2 In Situ Reservoir Pressure Gradients Discussion

A 100% brine-filled reservoir is assumed for the dynamic flow model. If hydrostatic conditions are also assumed, then the initial reservoir pressure will be equal to the weight of the fluid column. McCain's correlation (McCain, 1991) is used to calculate the density of brine at reservoir conditions. A salinity of 125,000 ppm is used in the equation, resulting in a brine density of 65.92 lb/ft^3, or 0.465 psi/ft. The midpoint of the injection zone is chosen to provide an average value. This pressure is then used to initialize the reservoir simulation at the midpoint, where tNavigator internally calculates pressures in each grid cell based on salinity and temperature at various points. Equations 3 and 4 provide a step-by-step guide in the brine density calculations.

(Eq. 3)
$$\rho_w = 62.368 + (0.4386 \times S) + (0.001600074 \times S^2)$$
$$\rho_w = 62.368 + \left(0.4386 \times \frac{125{,}000}{10{,}000}\right) + \left(0.001600074 \times \frac{125{,}000}{10{,}000}^2\right)$$
$$\rho_w = 66.67\ lb/ft^3$$

Where:
ρ_w = density of brine
S = total dissolved content of brine, expressed as weight percent

(Eq. 4)
$$\rho_w\ @\ Reservoir\ Conditions = \frac{\rho_w\ @\ Reservoir\ Conditions}{B_w}$$
$$\rho_w\ @\ Reservoir\ Conditions = \frac{66.67}{1.0114}$$
$$\rho_w\ @\ Reservoir\ Conditions = 65.92\ lb/ft^3$$

Where:
ρ_w = density of brine
B_w = volume formation factor of brine

2.5.2.3 Injection Zone Fracture Gradient Calculation

The fracture pressure is a function of Poisson's ratio (v), overburden gradient (OBG), and pore gradient (PG). Eaton's method (Eaton, 1968) is used to calculate the pressure required to fracture the injectable rock. Primarily developed using data from Gulf Coast sands, this method offers a practical means of estimating the fracture pressure of the rock. Eaton's method is recognized as a standard practice in the industry, contributing to the assessment and optimization of hydraulic fracturing operations in various geological settings. Table 2-3 provides the values of each input.

Table 2-3 – Injection Zone Fracture Gradient Calculation Assumptions – Eaton's Method

Inputs	Values
Poisson's Ratio	0.339
Overburden Gradient (psi/ft)	0.92
Pore Gradient (psi/ft)	0.465

Poisson's ratio was determined through an extensive literature review on unconsolidated sandstones. Literature suggests that sandstones can have a wide range of potential Poisson's ratios (0.1–0.4). The review primarily focused on sandstones that closely resemble the unconsolidated nature of the Miocene sands. Further research showed that soft sandstones can have a range of 0.2–0.35 (Molina, Vilarrasa, and Zeidouni, 2017). A study conducted by Eaton (1968) also suggests that the Gulf Coast sands will tend to have a Poisson's ratio greater than 0.3 at the respective depths.

Geomechanical analysis was also conducted on a nearby sonic log (SN 223134) to determine Poisson's Ratio. The analysis yielded a Poisson's ratio of 0.339 for the injectable sands, which corresponds with estimates from literature. A value of 0.339 was chosen to be the most representative of the Gulf Coast sands, based on the literature and site-specific data. Figure 2-24 provides the estimated Poisson's Ratio from SL 15475 (SN 223134) sonic log.

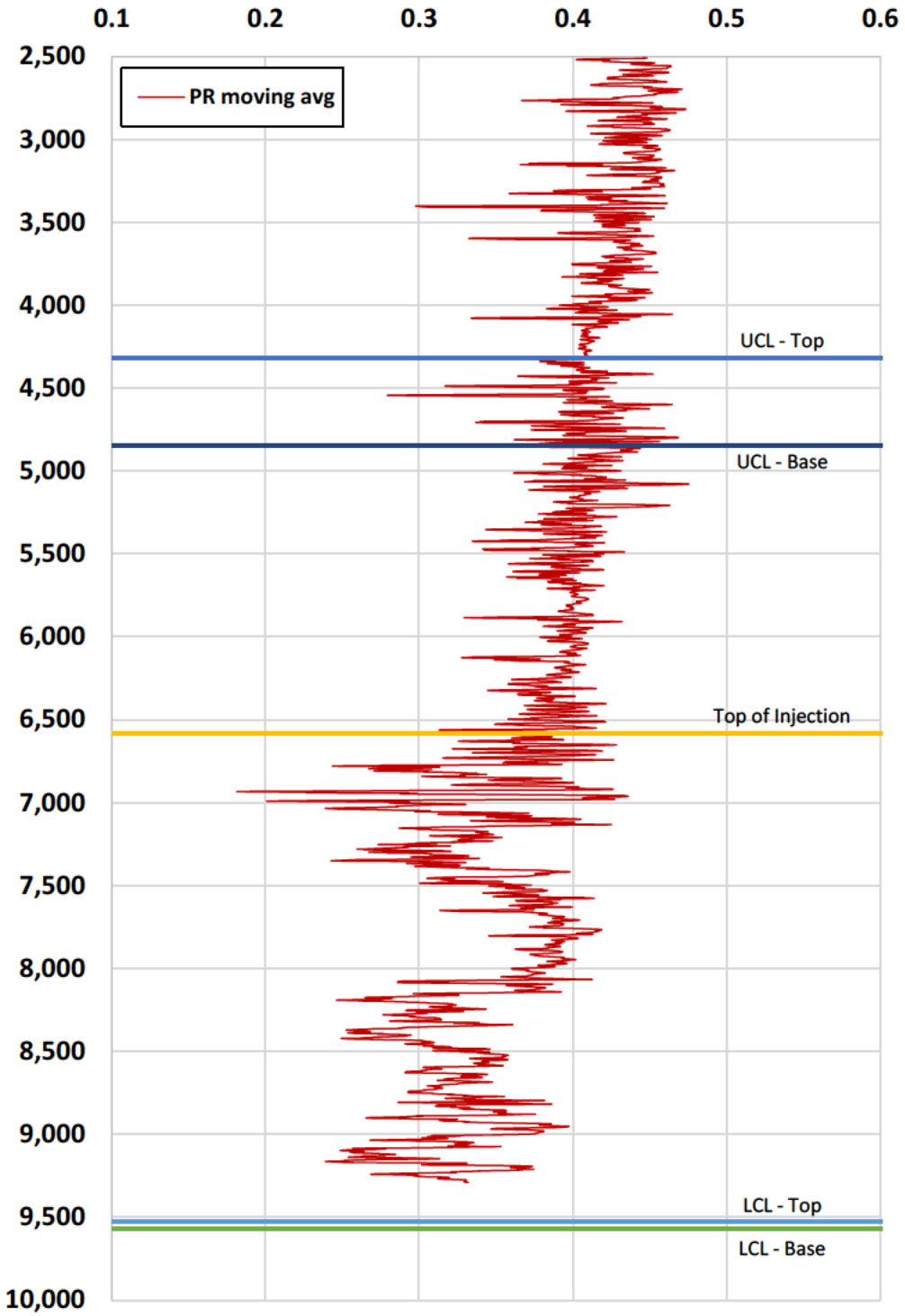

Figure 2-24 – Estimated Poisson's Ratio from Sonic Log (SN 223134)

Public literature was utilized to determine the OBG of the target formation. Figure 2-25 shows a composite OBG for the Gulf Coast at various depths (Eaton, 1968). A value of 0.92 psi/ft was chosen to best represent the OBG in this area. A PG of 0.465 psi/ft was calculated from the salinity estimates as discussed in Section 2.5.2.2.

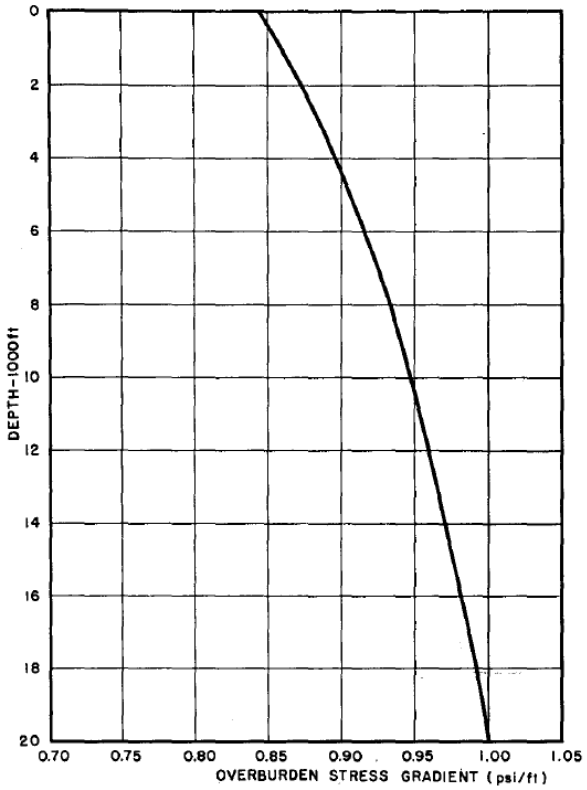

Figure 2-25 – Composite Overburden Stress Gradient for Gulf Coast Formations (Eaton, 1968)

The inputs are used to calculate the fracture gradient (FG). Equation 5 highlights the steps for calculating the gradient. Per SWO 29-N-6 **§3621.A.1** [40 CFR **§146.88(a)**], the well may not exceed 90% of the fracture gradient of the injection zone during injection operations. Therefore, the model applied a pressure constraint of 0.628 psi/ft to all injectors.

(Eq. 5)

$$FG = \frac{\nu}{1-\nu}(OBG - PG) + PG$$

$$FG = \frac{0.339}{1-0.339}(0.92 - 0.465) + 0.465$$

$$FG = 0.698\ psi/ft$$

$$FG\ with\ Safety\ Factor = 0.698 \times 0.9 = 0.628\ psi/ft$$

2.5.2.4 Reservoir Fluid Properties

Reservoir Temperature

A review of nearby well logs and regional literature was conducted to estimate the reservoir temperature. First, public literature was used to gain insight into the regional temperature trends. The study showed that the geothermal gradient changes with depth, and data was therefore looked at in 5,000-ft intervals. Spoonbill No. 001 through 005 are situated in St. Charles Parish. Figure 2-26 provides a snapshot of the average geothermal gradients in those parishes at the target formation depths.

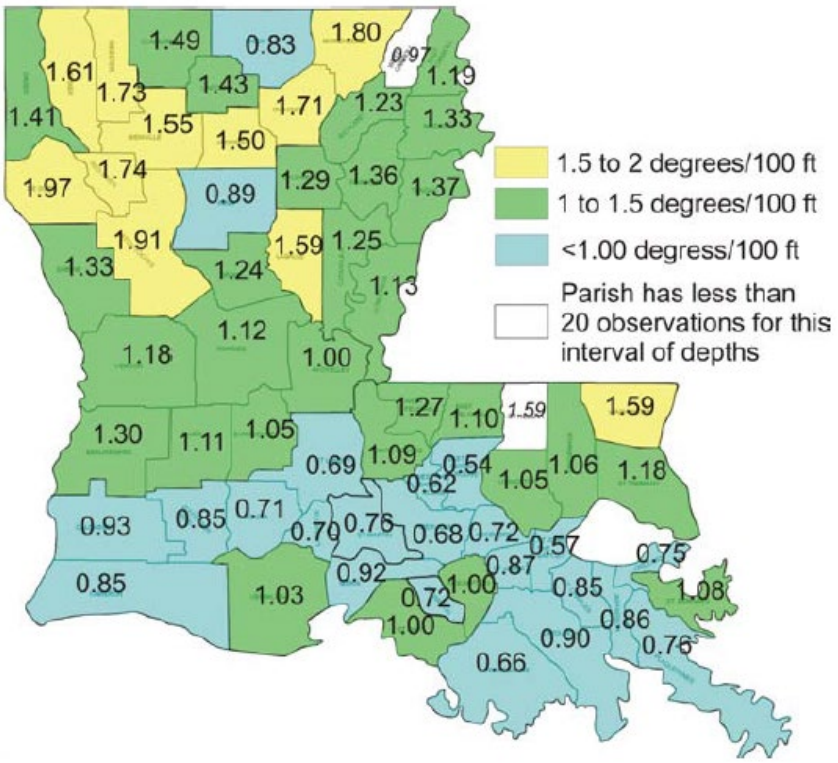

Figure 2-26 – Geothermal Gradients in Louisiana Parishes from Depths of 5,000 to 10,000 ft (Carlson and McCulloh, 2006)

Well logs were also reviewed near the injection sites to determine site-specific temperature gradients. From this review, the nearest well log was chosen to provide the most analogous data point to the target formation. The reservoir temperature gradient was estimated to be 0.98°F/100 ft, based on the average temperature gradient derived from the offset well review. This gradient is in line with the regional data, providing an increased confidence interval. That gradient is added to an assumed surface temperature of 72°F, which is the mean annual surface temperature. Figure 2-27 provides the offset well logs and their associated temperature gradients.

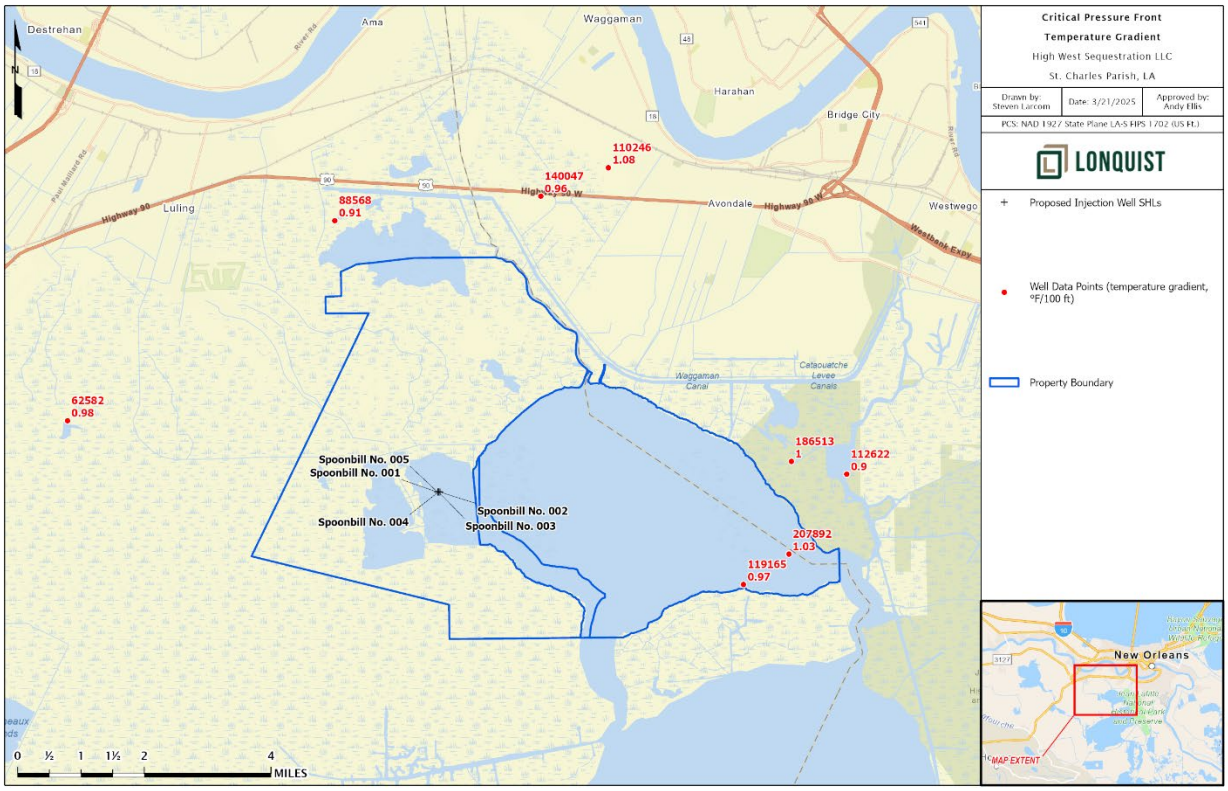

Figure 2-27 – Offset Logs Used for Reservoir Temperature Review

Brine Salinity

Regional salinity trends within the target reservoir were identified through a comprehensive review of published fluid samples. Fluid data was extracted from the US Geological Survey (USGS) National Produced Waters Geochemical Database (Blonde, 2018), a comprehensive online repository of water samples aimed at improving the regional hydrological interpretations. Fluid samples collected in Jefferson, Lafourche, Plaquemines, and St. Charles Parishes were analyzed to identify any discernible trends within the injection zone. Figure 2-28 highlights the total dissolved solids (TDS) content for each sample, revealing notable variability in salinity within the injection zone. The brine within the target appears to have an approximate range of 2,300 milligrams per liter (mg/L) to 225,000 mg/L.

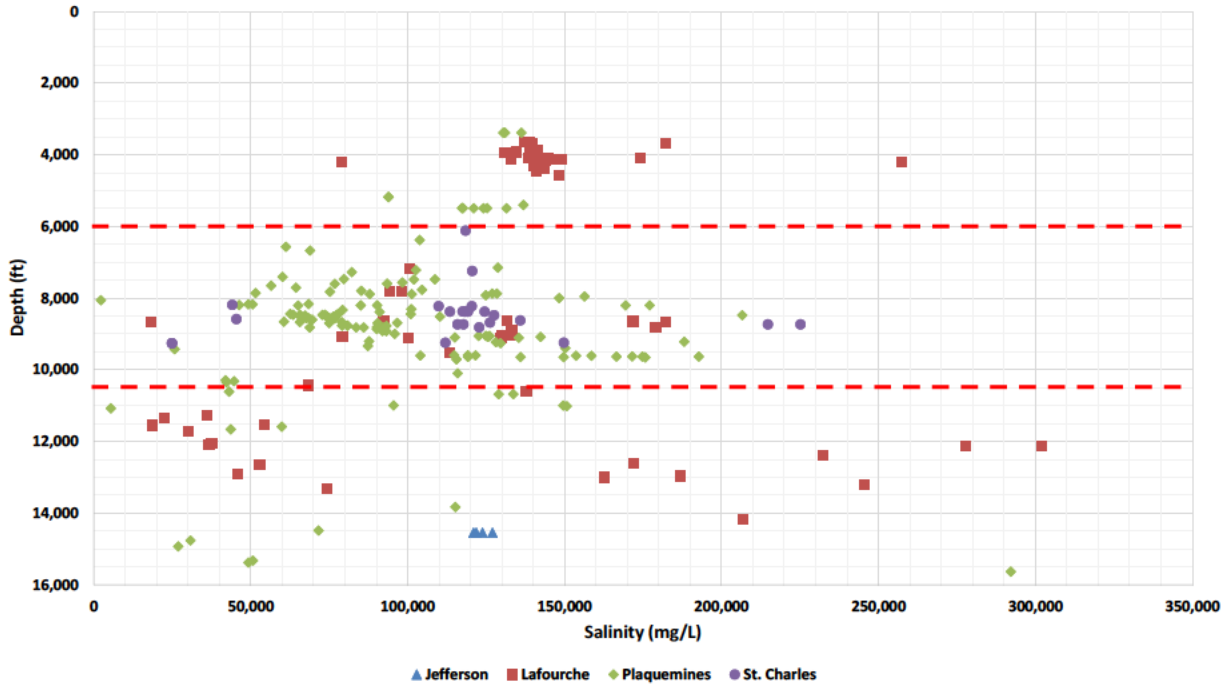

Figure 2-28 – TDS Content from USGS Produced Waters Database (Blonde, 2018)

Based on the regional data, the salinity was estimated to be 125,000 ppm. This value falls within the range seen in the regional samples, further confirming the dataset. The model was initialized with the calculated salinity value of 125,000 ppm.

2.5.3 Rock Properties Hysteresis Modeling

2.5.3.1 Rock Compressibility

In absence of regional and site-specific data, published literature was utilized to determine rock compressibility. A targeted review of published literature on unconsolidated, poorly sorted sandstones was conducted. The research indicates that some formations, such as unconsolidated sandstones, may exhibit a wide range of compressibility values (Newman, 1973). Figure 2-29 represents the class averages for each rock type in porosity increments of 5% where he values approximately range between 10-40 microsips (Newman, 1973). This range is consistent with the results of the Frio Brine Pilot Experiment study, which calculated a compressibility of 3×10^{-9} Pa^{-1} (20.7 microsips) from well tests in the Frio formation (Hovorka et al., 2003). For the simulation, a representative value of 25 microsips was selected for the injection interval. This assumption is subject to revision pending the acquisition of data from the stratigraphic test well and/or proposed injection wells.

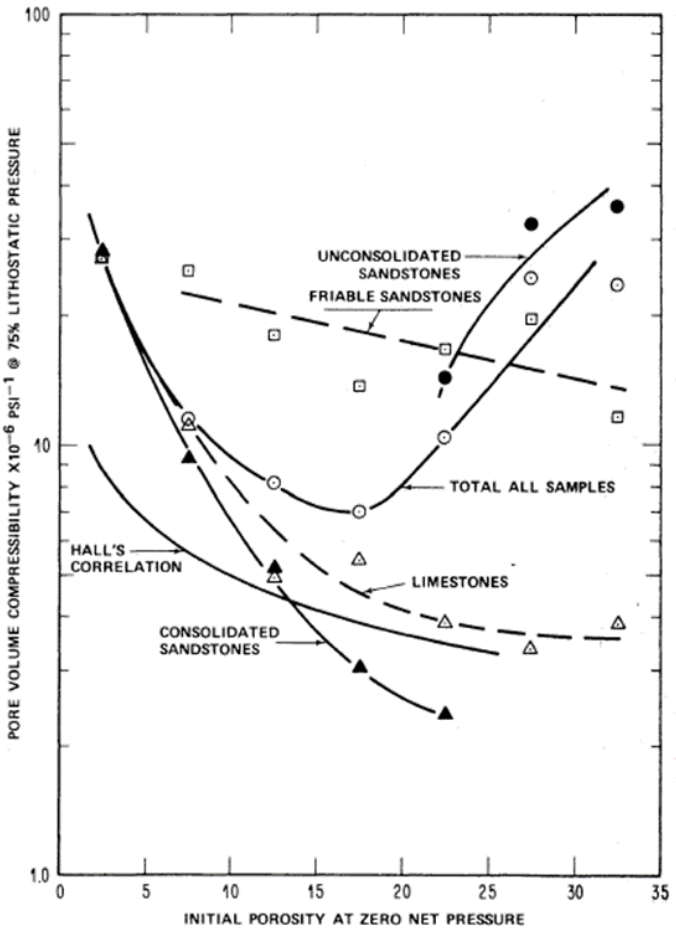

Figure 2-29 – Pore-Volume Compressibility vs. Initial Sample Porosity (Newman, 1973)

2.5.3.2 Residual Gas Saturation

Residual gas saturation (S_{gr}) refers to the amount of supercritical CO_2 that can be residually trapped in the pore space. Public literature was utilized to determine the input, as no site-specific data has been collected yet. From a review of multiple sources (Hovorka et al., 2003; Holtz, 2005; Bachu and Bennion, 2008; Bachu, 2012), the S_{gr} values can range from 10 to 40% in sandstones. The model uses a value of 30%**,** as it best represents the Gulf Coast sandstone as seen in Figure 2-30. This figure portrays 144 data points from samples across the globe, including four samples taken from the Frio, an analogous depositional environment.

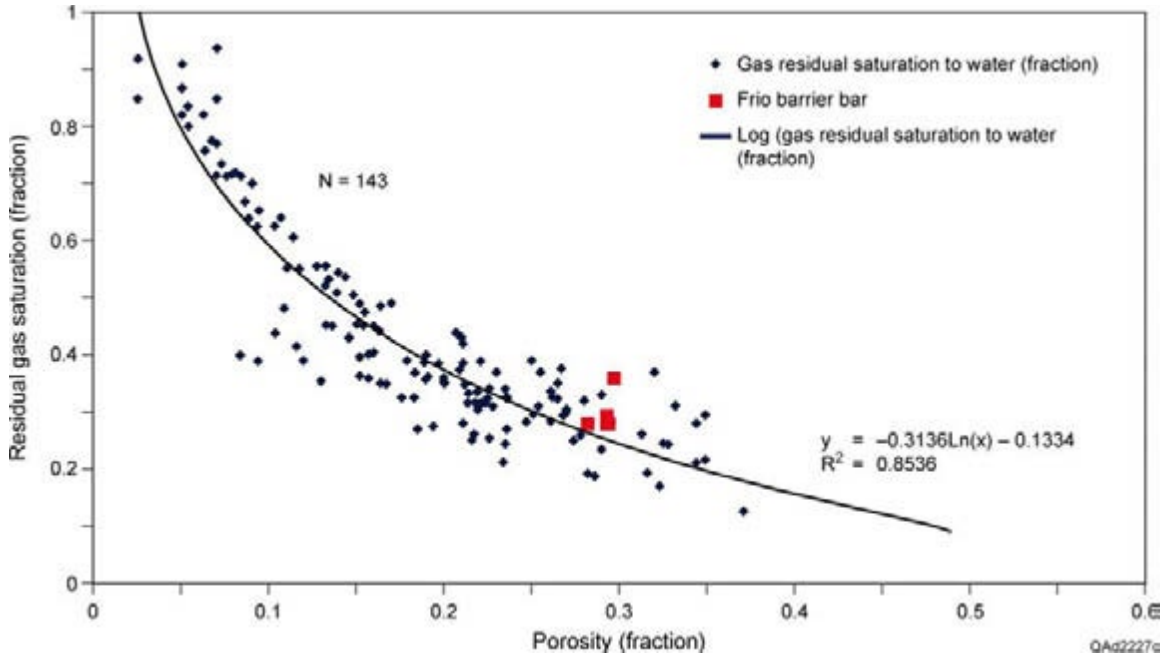

Figure 2-30 – Comparison of S_{gr} samples taken from the Frio Sands vs. published literature (Hovorka et al., 2003)

Site-specific core acquisition and analysis is planned with a stratigraphic test well and/or upon completion of the subject injection wells. The model inputs will be updated as new data is acquired.

2.5.3.3 Relative Permeability Curves

In the absence of site-specific data, relative permeability curves were generated using research findings from analogous depositional environments. Traditional core testing faces challenges in accurately determining curve endpoints, leading to elevated irreducible water saturations (S_{wirr}) and lower CO_2 endpoints (Benson, 2013). In the drainage CO_2-brine relative-permeability experiments, as the water saturation decreases, the capillary pressure (P_C) values increase rapidly as P_C approaches the irreducible water saturation. The high mobility ratio limits the necessary capillary pressure required to achieve high saturations of CO_2 during the test. This phenomenon causes the experimental relative-permeability measurements to end at water saturations higher than the actual irreducible water saturation.

Corey-Brooks equations were utilized to generate drainage curves for the sand and shale facies. The necessary inputs for solving these equations were determined through a comprehensive review. In this process, the irreducible water saturation was assumed to be 15.4% and 40%, for the sand and shale facies, respectively. The sand and sandy-shale facies assumed CO_2 permeability endpoints of 1 and 0.65 for both brine and CO_2 curves, respectively. Fitting these assumptions to data from various references (Krevor et al., 2012) yielded brine and CO_2 exponents of 5 and 4, respectively. For the shale facies, 1 and 0.5 were assumed to be the brine and CO_2 endpoints, respectively. The shale facies have CO_2 and brine exponents of 6.5 and 2.6. Subsequently, imbibition curves were internally calculated in tNavigator using the Carlson and

Land method. Figure 2-31 and Figure 2-32 visually present the drainage and imbibition curves employed in both models.

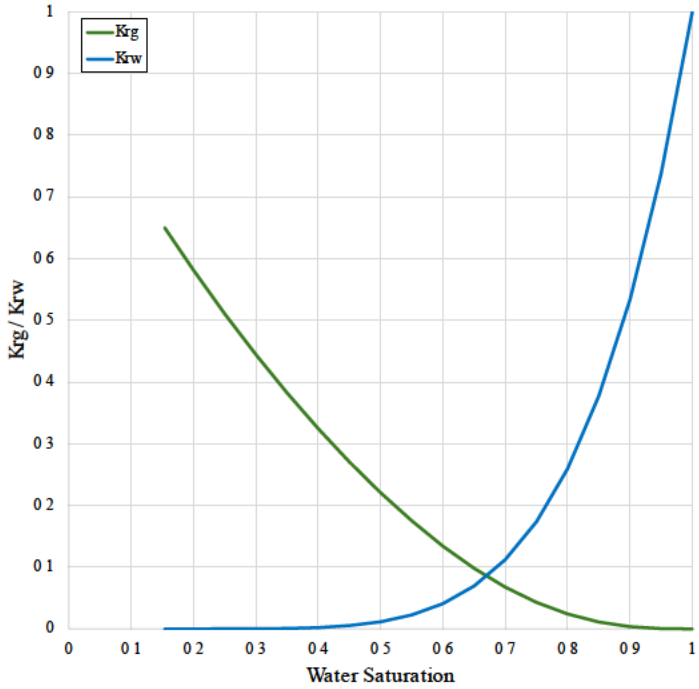

Figure 2-31 – Two-Phase Relative Permeability Curves for Sand and Sandy-Shale Facies

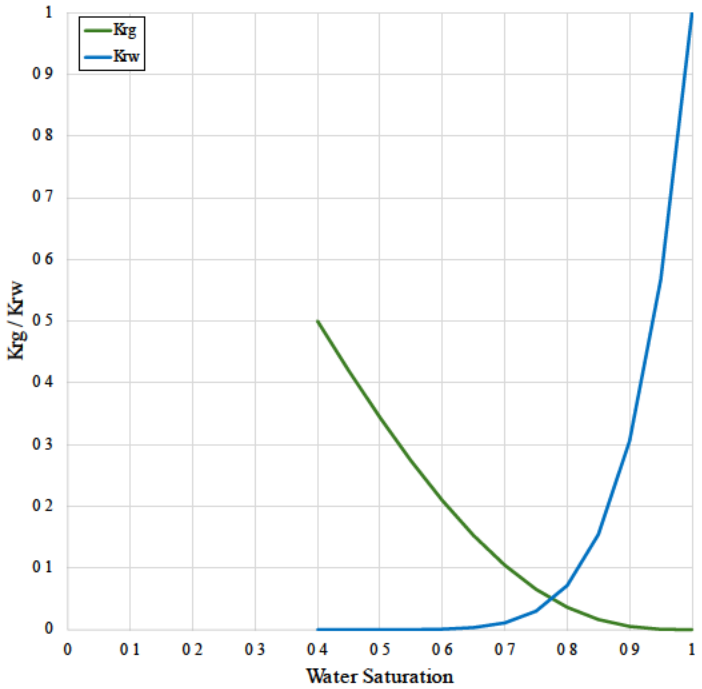

Figure 2-32 – Two-Phase Relative Permeability Curves for Shale Facies

Site-specific core acquisition and analysis is planned with a stratigraphic test well and/or upon drilling and completion of the subject injection wells. The model and subsequent curves will be updated after the core data has been analyzed.

2.6 Wellbore Hydraulics Parameters

The wellbore parameters remained the same for each injector. The wellbore configuration in the model was set up using the proposed well design and incorporated additional assumptions specified in Table 2-4. In tNavigator, three primary constraints were imposed to limit the supercritical CO_2 front growth and pressure response: (1) a maximum injection rate of 1.5 to 2.5 MMT/yr, (2) a maximum bottomhole pressure (BHP) gradient of 0.711 psi/ft, and (3) an injection duration of 20 years, for all wells. The maximum injection rate and duration constraints were selected to maximize storage capacity in the available pore space. The maximum BHP constraint was determined through calculations discussed in *Section 2.5.2.3*, on the fracture gradient calculation.

Table 2-4 – Wellbore Hydraulics Parameters

Inputs	Values
Maximum Injection Rate (MT/yr)	1,500,000 – 2,500,000
Pressure Gradient Constraint (psi/ft)	0.628
Injection Duration (yrs)	20
Tubing Inner Diameter (in.)	6.054
Tubing Setting Depth (ft)	4,398
Roughness Factor	0.0000656
Wellhead Temperature (°F)	90

The Gulf Coast system presents a unique depositional environment where interbedded shales may act as barriers that impede CO_2 migration. To optimize pore space utilization, the formation was split into five zones. A single pad will be constructed with five wells that will each target separate zones within the injection formation. These zones are strategically designed to leverage the shale barriers, to control and mitigate the supercritical CO_2 plume expansion. The BHP constraint for injection well is adjusted for each upper perforation depth to prevent the BHP from exceeding the calculated fracture gradient. This measure ensures a safe and effective injection process. A summary of each completion zone for each supercritical CO_2 injector is provided in Table 2-5.

Table 2-5 – Completion Strategy

Well No	Top Perf (ft)	Gross Thickness (ft)	Net Pay (ft)	Duration (yrs)
001	9,725	360	303	20
002	8,703	771	534	20
003	8,160	512	409	20
004	7,036	878	466	20
005	6,129	815	660	20

Figure 2-33 provides a visual representation of Table 2-5. The dashed lines represent the upper and lower structural horizons from the imported geologic model. The black triangles represent the net pay that was completed for each proposed injection well.

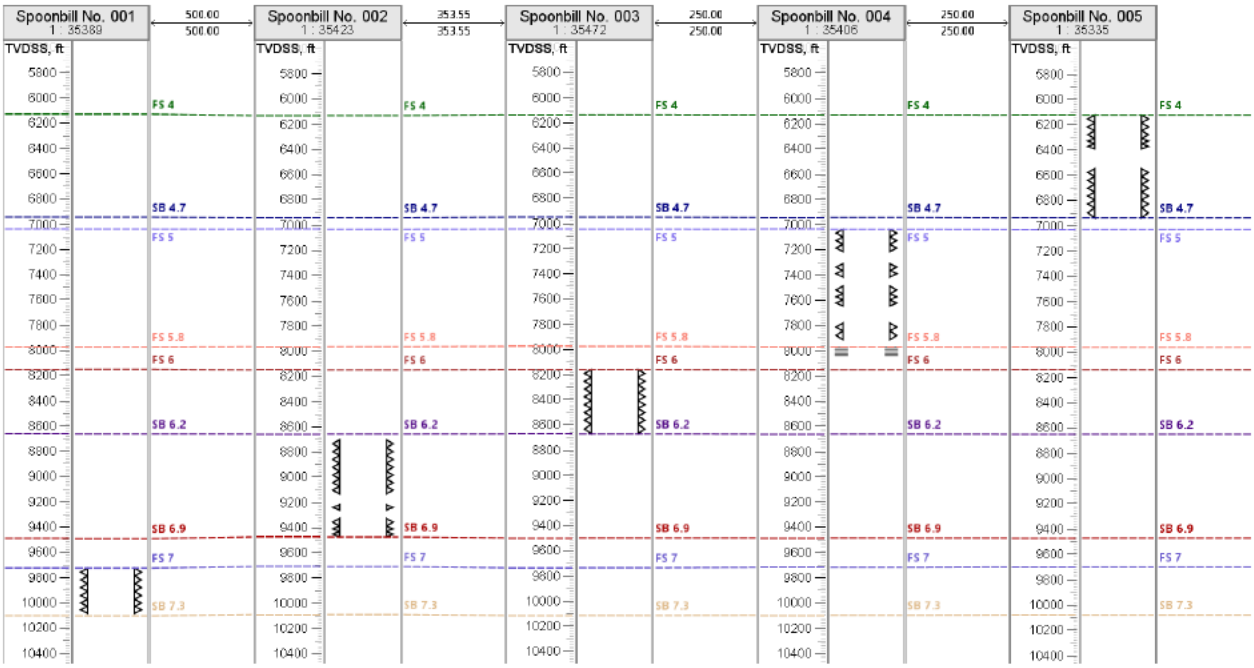

Figure 2-33 – Modeled Well Log Cross Section

To estimate surface injection pressure, tNavigator utilizes vertical flow performance (VFP) curves. The VFP curves are generated by creating a wellbore model to predict pressure drop through the tubulars. Furthermore, tNavigator's heat transfer module was enabled as a key input to simulate any heat loss/gain in the wellbore due to heat exchange between the injected fluid and reservoir. This module allows the model to more accurately calculate the phase density and pressure drop through tubing. Figure 2-34 highlights the injection stream temperature along the wellbore (Spoonbill No. 001) that was used as an input in the heat transfer module.

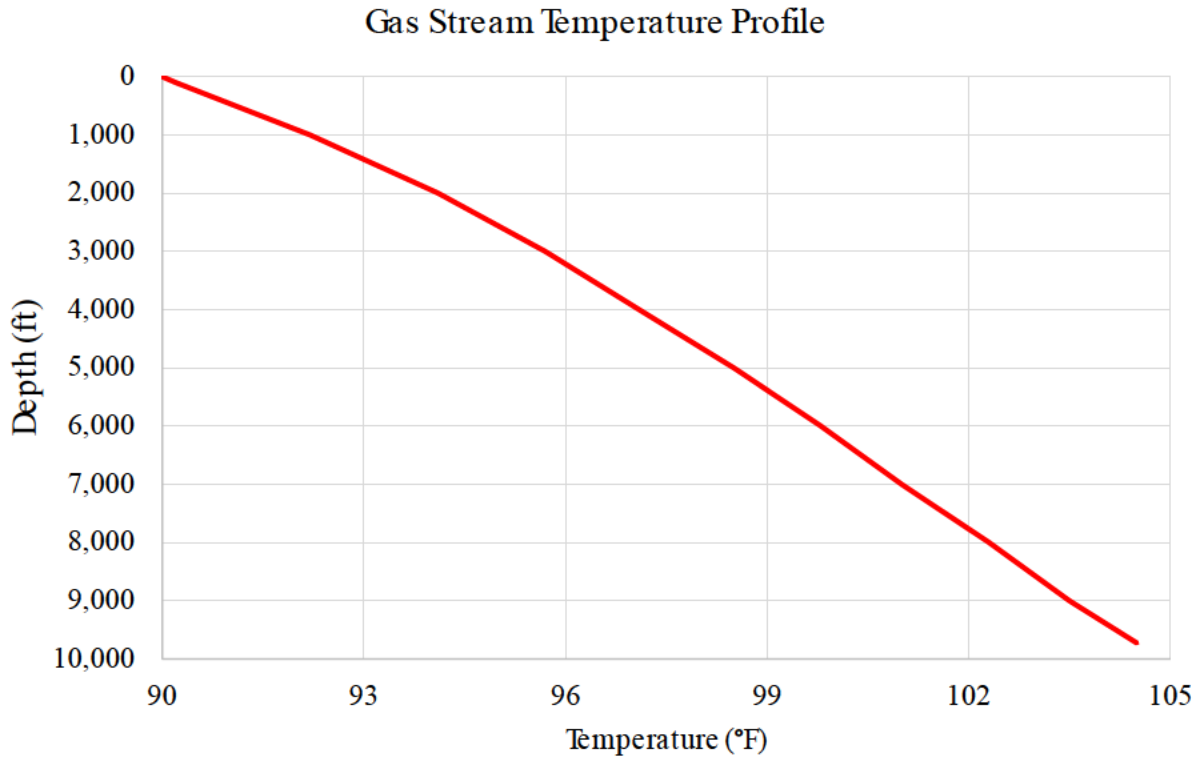

Figure 2-34 – Injection Stream Temperature along Wellbore for Spoonbill No. 001

2.7 Model Results

2.7.1 Active Injection Operations of Proposed CO_2 Injector

The injection rate and pressure response due to CO_2 injection are outputs from the dynamic model in tNavigator. The maximum rates for Spoonbill No. 001, 003, and 004 are held to 2.0 MMT/yr for the life of each well (20 years). The maximum rate for Spoonbill No. 002 and 005 is held to 1.5 MMT/yr and 2.5 MMT/yr, respectively. The BHP is calculated internally by tNavigator and does not exceed the pressure constraint imposed on the model. This constraint prevents the BHP from exceeding 90% of the fracture gradient as required by SWO 29-N-6, **§3621.A.1** [40 CFR **§146.88(a)**]. This pressure constraint is critical to the model's design, ensuring regulatory compliance and responsible subsurface management.

The initial surges or "spikes" in the BHP response at the beginning of each stage primarily stem from two factors: relative permeability curve behavior and numerical discretization effects within the dynamic model. Due to the model's use of finite difference equations to approximate fluid flow between relatively large grid blocks, the introduction of supercritical CO_2 results in an initial overestimation of the pressure response. However, once supercritical flow is stabilized, the reservoir pressure subsequently returns to the anticipated values. Figures 2-34 through 2-38 highlight the proposed injection wells' BHP response and injection.

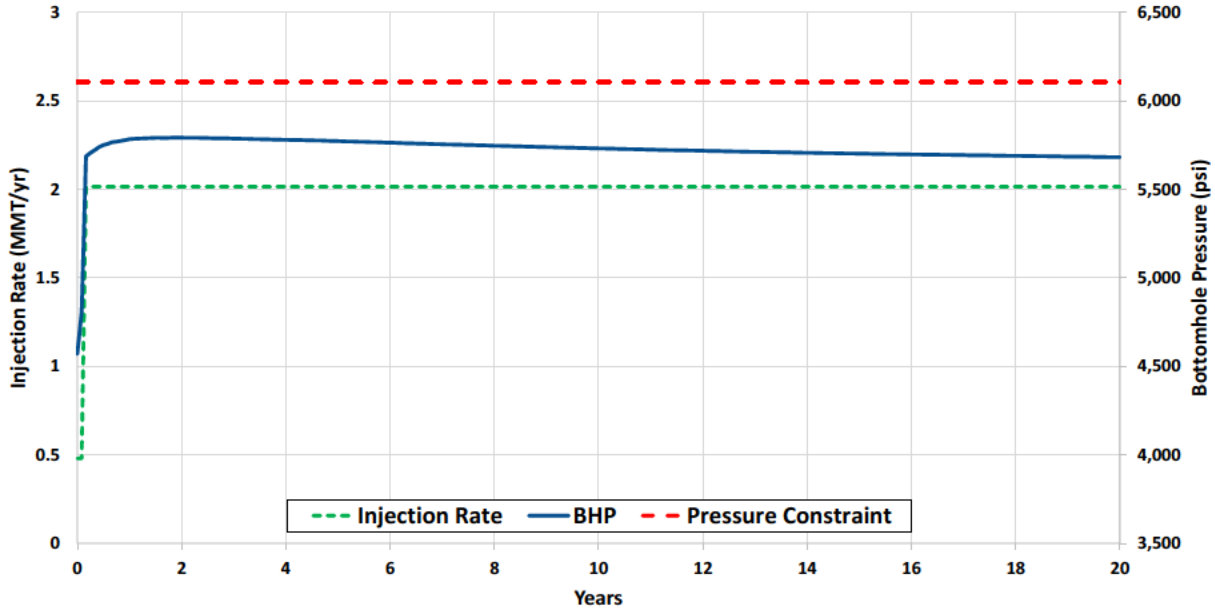

Figure 2-35 – Wellbore Model Outputs During Active Injection Period for Spoonbill No. 001

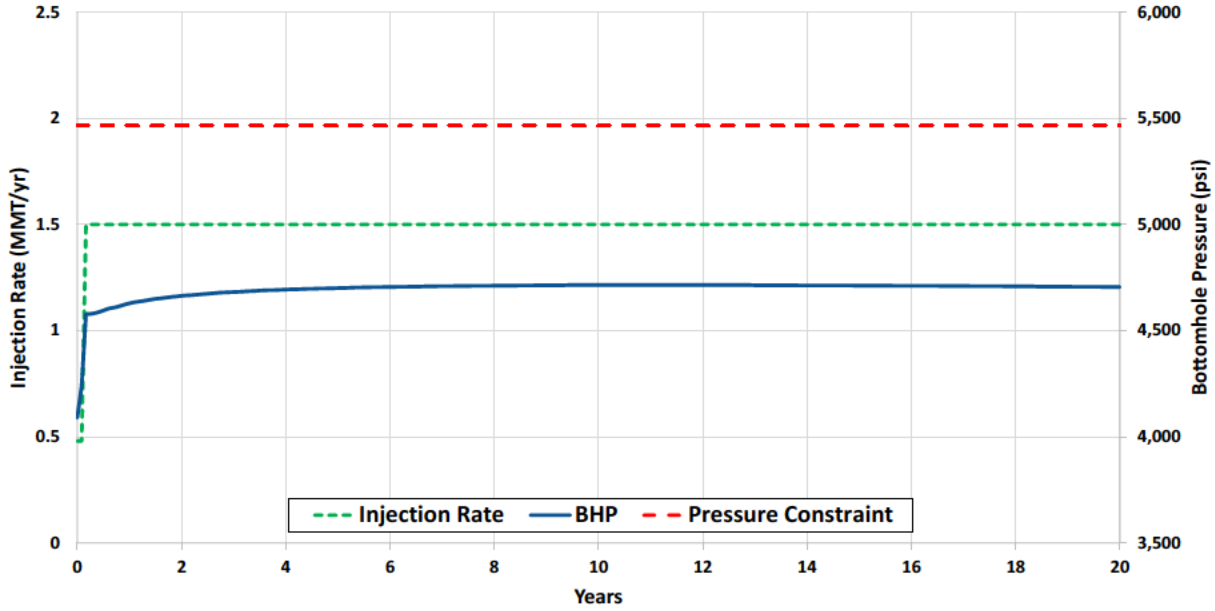

Figure 2-36 – Wellbore Model Outputs During Active Injection Period for Spoonbill No. 002

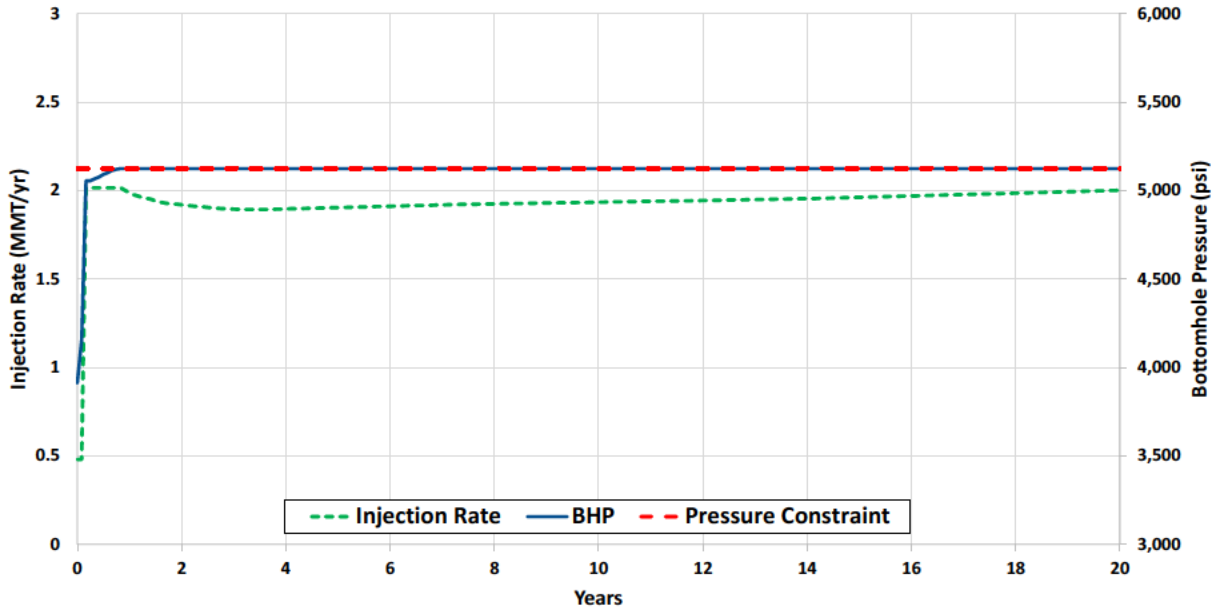

Figure 2-37 – Wellbore Model Outputs During Active Injection Period for Spoonbill No. 003

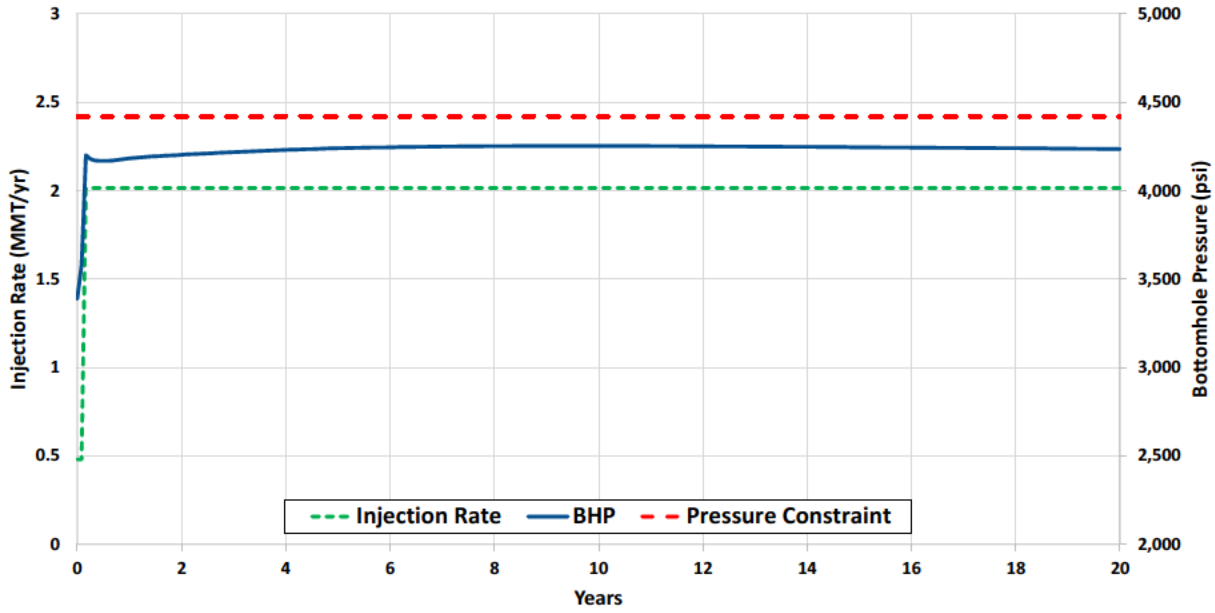

Figure 2-38 – Wellbore Model Outputs During Active Injection Period for Spoonbill No. 004

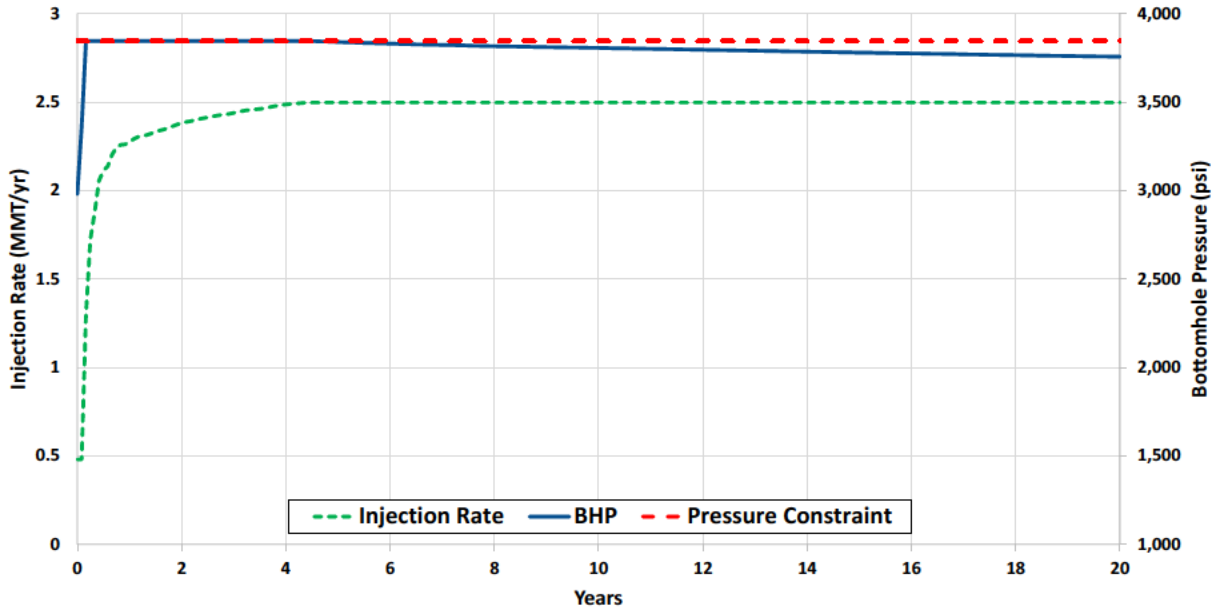

Figure 2-39 – Wellbore Model Outputs During Active Injection Period for Spoonbill No. 005

tNavigator uses VFP curves to determine the WHP based on the BHP response. The inputs and construction of the wellbore model are discussed in Section 2.6. Once the model is built, tNavigator offers multiple correlations to choose from that will predict the pressure drop through tubing for both single phase and multi-phase flow. In the presence of a single-phase fluid regime, the Moody correlation (Moody, 1947) was selected. For multiphase flow in vertical segments of the well, the Hagedorn and Brown Correlation (Hagedorn & Brown, 1965) was selected, while the Beggs and Brill Correlation (Beggs & Brill, 1973) was chosen for the deviated segments of the wellbore. The resulting chart is shown in Figure 2-39 where representative VFP curves are implemented for each wellbore.

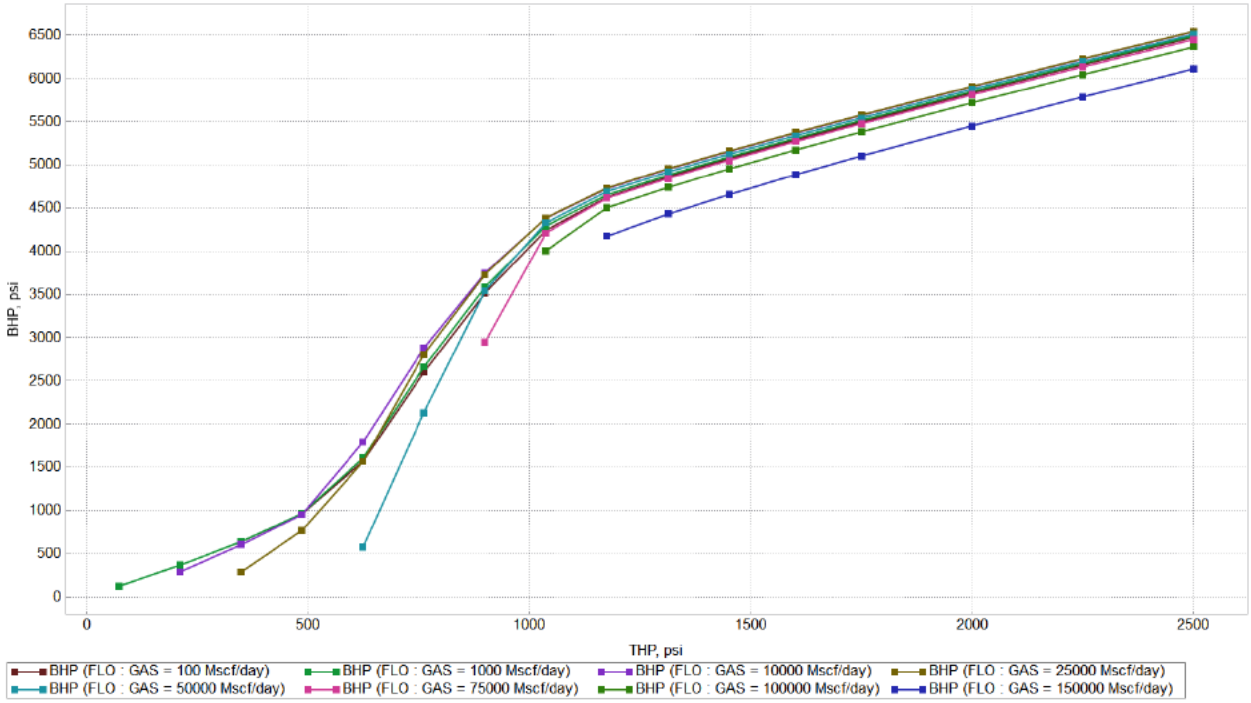

Figure 2-40 – Representative VFP Curves

The maximum expected BHP of Spoonbill No. 005 to No.001 is estimated to be 3,845 to 5,793 psi during the life of the project, evaluated at 9,725 ft. On average, the BHP of all wells will be between 3,803 and 5,729 psi. The maximum WHP for all injectors is calculated to be 1,532 to 2,078 psi with an average of approximately 1,519 to 2,049 psi. Table 2-6 highlights the outputs for each injection well as modeled in tNavigator.

Table 2-6 – Spoonbill No. 001 to 005 Outputs

Well No.	Max Rate (MMT/yr)	Avg Rate (MMT/yr)	Max BHP (psi)	Avg BHP (psi)	Max WHP (psi)	Avg WHP (psi)
001	2.02	2.01	5,793	5,729	2,078	2,029
002	1.50	1.49	4,715	4,696	1,532	1,519
003	2.02	1.94	5,124	5,116	2,065	2,049
004	2.02	2.01	4,253	4,233	1,745	1,729
005	2.50	2.45	3,845	3,803	1,768	1,730

Injecting supercritical CO_2 into a saline aquifer causes "pressure buildup," defined as an increase in reservoir pressure above the in situ pressure. The magnitude of this pressure increase is greatest near the wellbore during the active injection period. Excessive and unmanaged pressure buildup can lead to several potential issues, including induced fracturing, fault reactivation, and leakage of CO_2 from the storage reservoir. To ensure the integrity of the injection site, the model imposes a pressure constraint equal to 90% of the frac gradient to ensure the safe storage of CO_2. The pressure buildup is monitored by the rise of reservoir pressure and its associated gradient based on the top of the perforated interval for each well.

Figures 2-40 through 2-44 illustrate the maximum pressure buildup at each well, calculated based on the BHP results representing the highest pressure observed within the reservoir at any specific time. Furthermore, as these pressure values are obtained at varying depths, the pressure gradient is also computed. The greatest buildup is experienced in Spoonbill No. 003, resulting in a 1,341-psi pressure increase. As shown in these Figures, the pressure gradient never exceeds the constraint of 0.628 psi/ft (90% of FG) imposed on the well, to allow for the safe injection of supercritical CO_2.

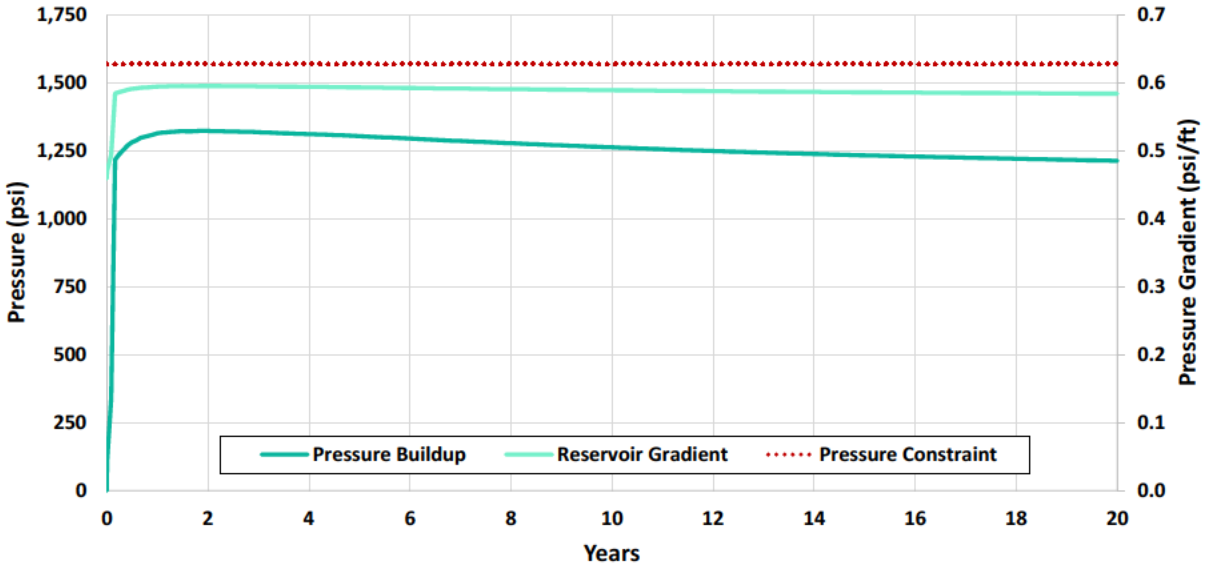

Figure 2-41 – Pressure Buildup During Active Injection Period for Spoonbill No. 001

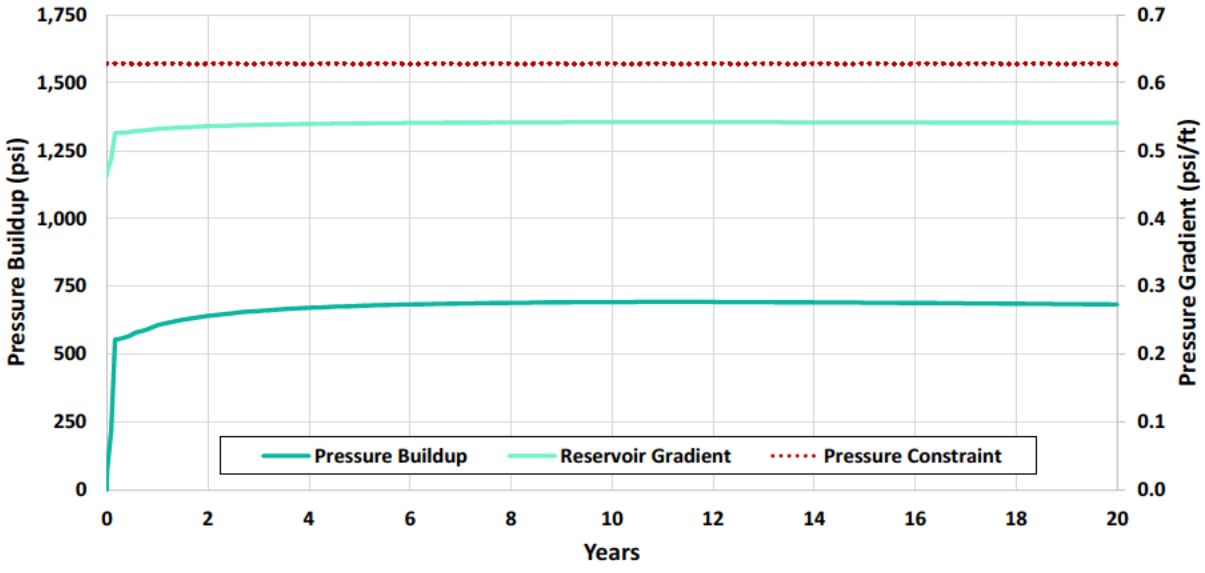

Figure 2-42 – Pressure Buildup During Active Injection Period for Spoonbill No. 002

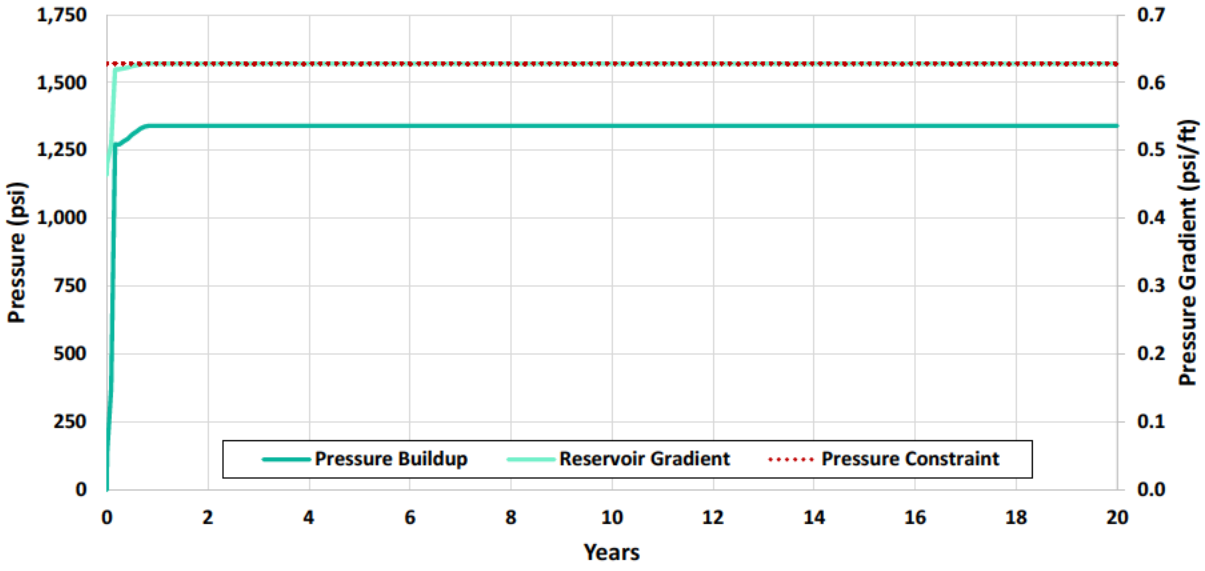

Figure 2-43 – Pressure Buildup During Active Injection Period for Spoonbill No. 003

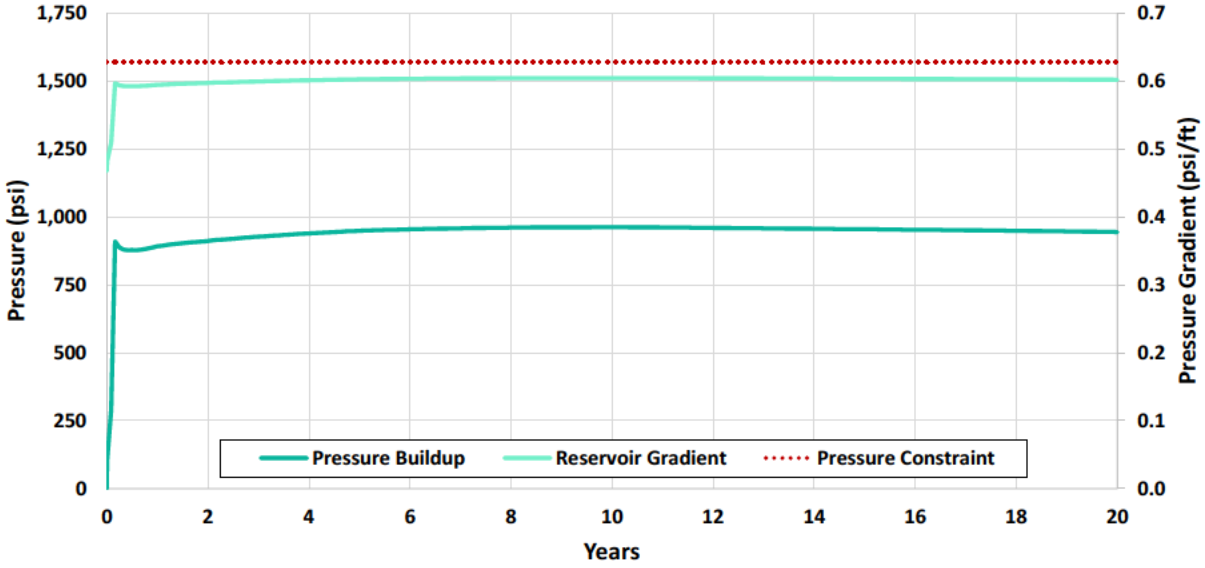

Figure 2-44 – Pressure Buildup During Active Injection Period for Spoonbill No. 004

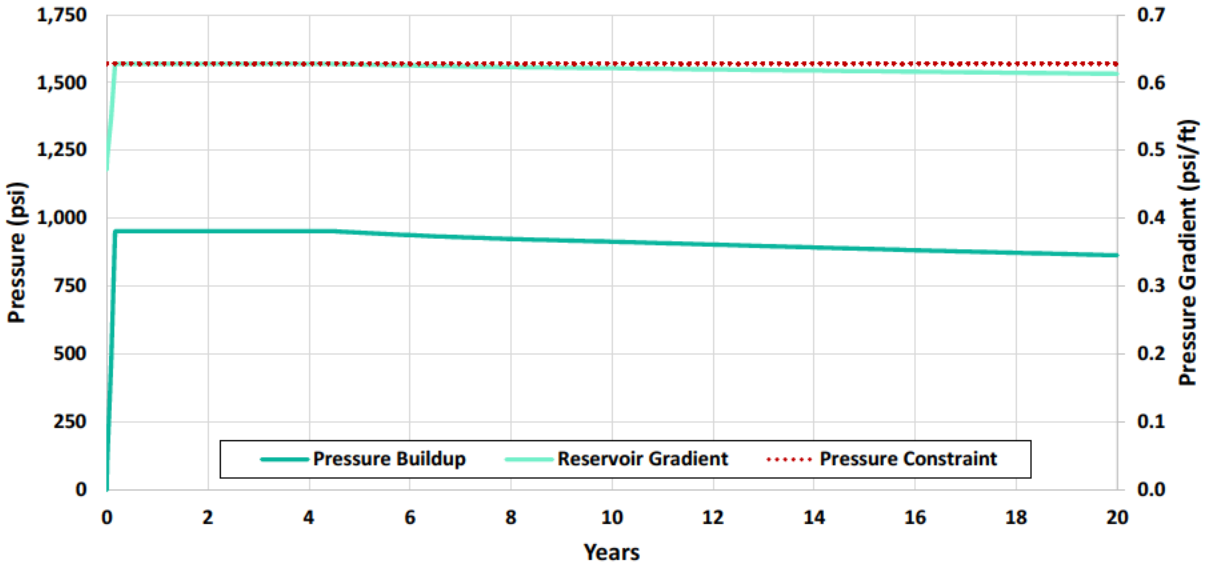

Figure 2-45 – Pressure Buildup During Active Injection Period for Spoonbill No. 005

The pressure buildup will begin to sharply decrease back to in situ conditions after injection operations conclude. Spoonbill No. 003 retains the highest pressure-buildup one year after the well is shut in, achieving a maximum increase of 334 psi. From there the pressure continues to decline until it reaches near in-situ conditions. Figure 2-45 highlights the pressure buildup for the entire life of Spoonbill No. 001. Figures 2-46 and 2-47 portray the east-west and south-north cross sections for the pressure increase, respectively.

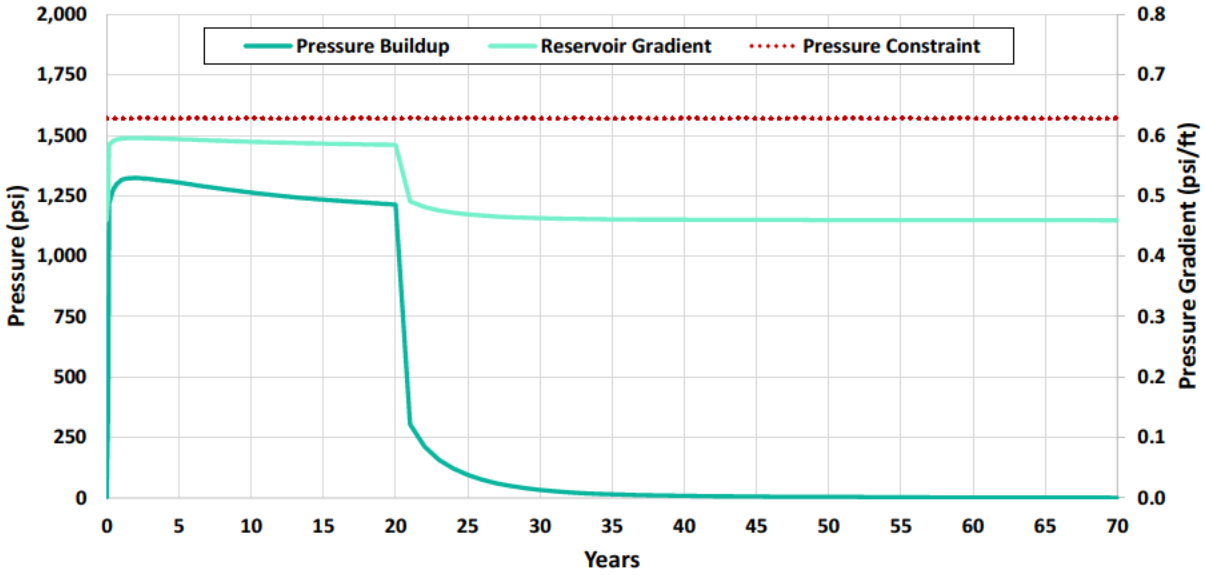

Figure 2-46 – Pressure Buildup During Life of Spoonbill No. 001

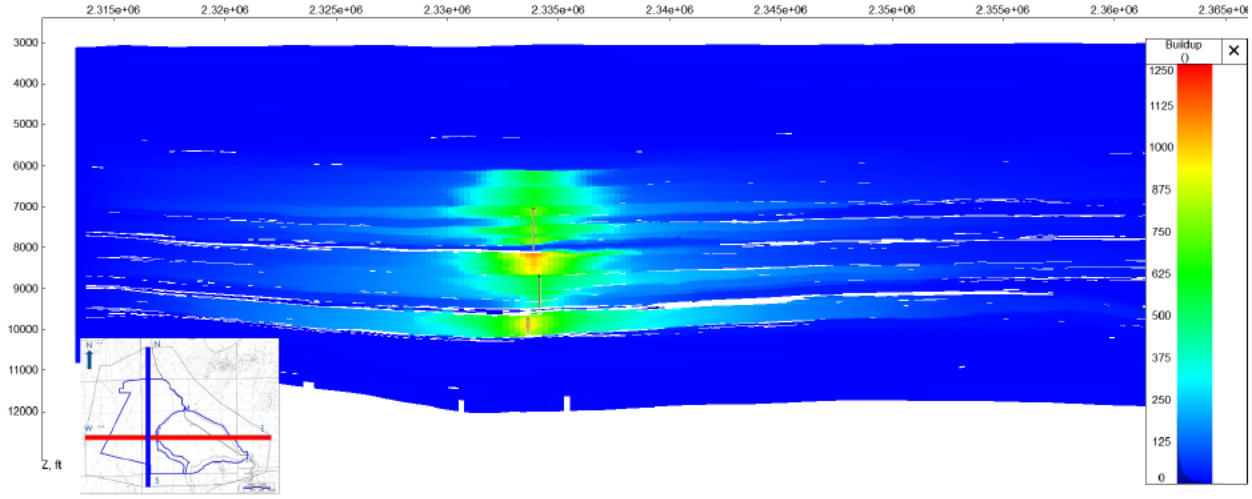

Figure 2-47 – West/East Cross Section of Pressure Buildup (Red Line on Inset Map)

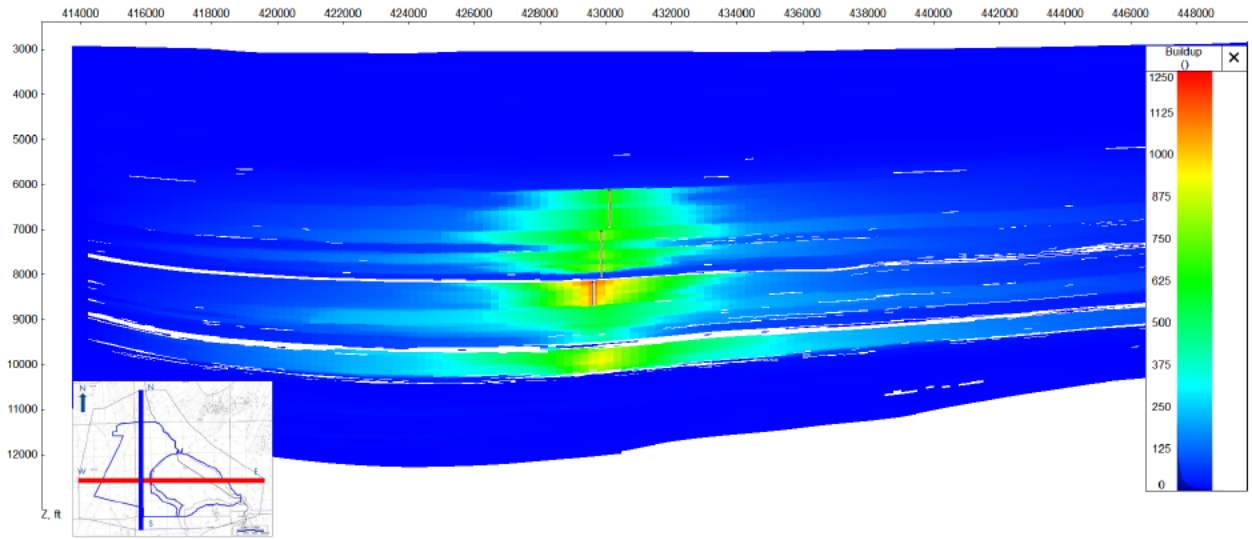

Figure 2-48 – South/North Cross Section of Pressure Buildup (Blue Line on Inset Map)

2.7.2 CO_2 Plume Migration for AOR Delineation

According to SWO 29-N-6 **§3615.B** [40 CFR **§146.84**], the AOR must be determined by the maximum extent of either the supercritical CO_2 front or the critical pressure front—or both. The first review starts with the extent of the CO_2 plume. The dynamic model was used to delineate the maximum carbon front. This section discusses the results of the model as it pertains to the delineation of the carbon front.

The CO_2 plume tends to migrate in the updip direction due to the buoyant nature of CO_2. However, the structure can vary from layer to layer in the model, resulting in multiple plumes migrating in various directions throughout the injection interval. This variation can be due to

structural changes, sand pinchouts, presence of channels, shale baffles, or other subsurface features. For example, channels are highly permeable sands that can act as "highways" for the CO_2 to preferentially migrate through. Overall, the CO_2 front migrates to the north from the injection sites.

Further examination of the cross sections of the plumes at the wellbore provides better insights into how the supercritical CO_2 migrates through the injection zone. As CO_2 is injected into each sand package, the subsequent plumes vary in size and shape. Between each sand package, interbedded clay-rich shales exist that help structurally trap CO_2 and inhibit vertical migration. The existing completion strategy is tailored to leverage these interbedded shales to help permanently sequester the CO_2 between completion intervals, while limiting the spatial extent of the plume. Figures 2-48 and 2-49 show the west/east and south/north cross sections of the CO_2 plume, respectively.

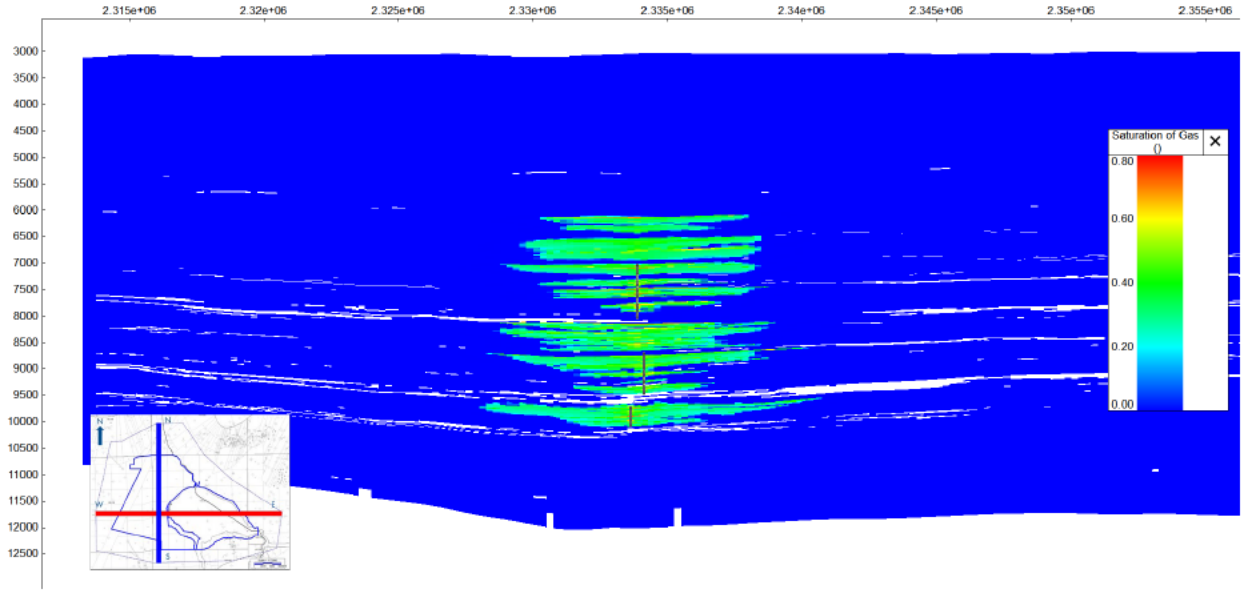

Figure 2-49 – West/East Cross Sections of Stabilized Free-Phase CO_2 Plume (Red Line on Inset Map)

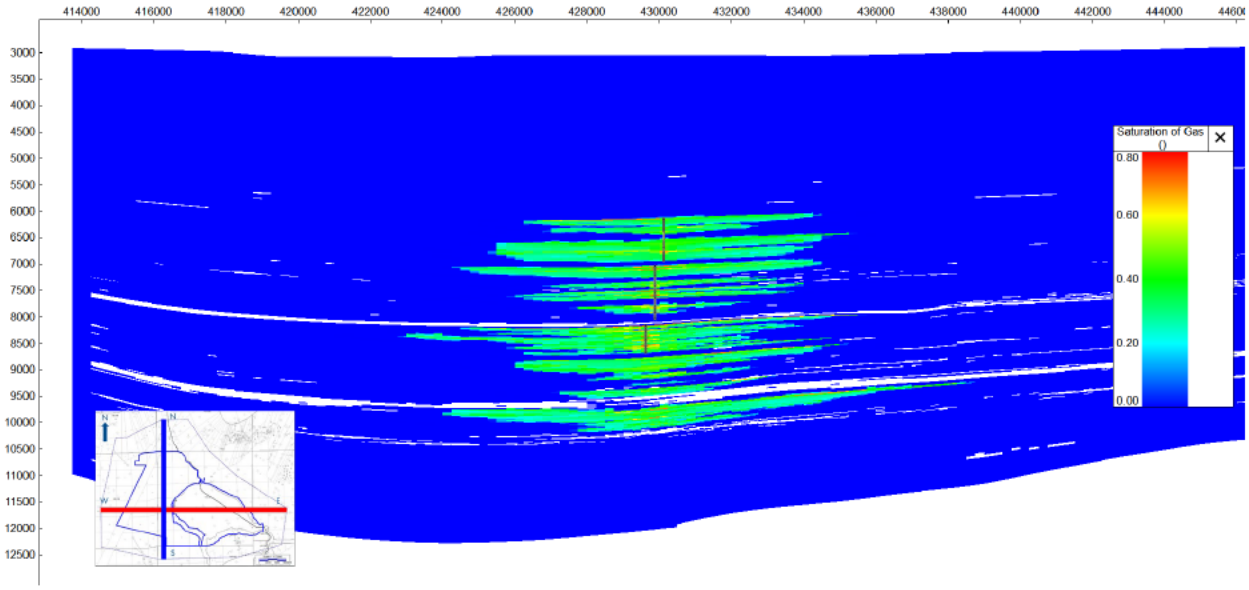

Figure 2-50 – South/North Cross Sections of Stabilized Free-Phase CO_2 Plume (Blue Line on Inset Map)

The CO_2 front is based on the most significant plume, or a combination of plumes from each completion. In the current dynamic model, the carbon front encompasses an area of 3,433 acres (~5.4 sq mi). The CO_2 front primarily extends to the north of the injection sites. The maximum diameter of the CO_2 plume is 2.83 mi, extending in the south-west west by north-east east (SWW-NEE) orientation. Figure 2-50 provides a visual representation of the maximum extent of the CO_2 front.

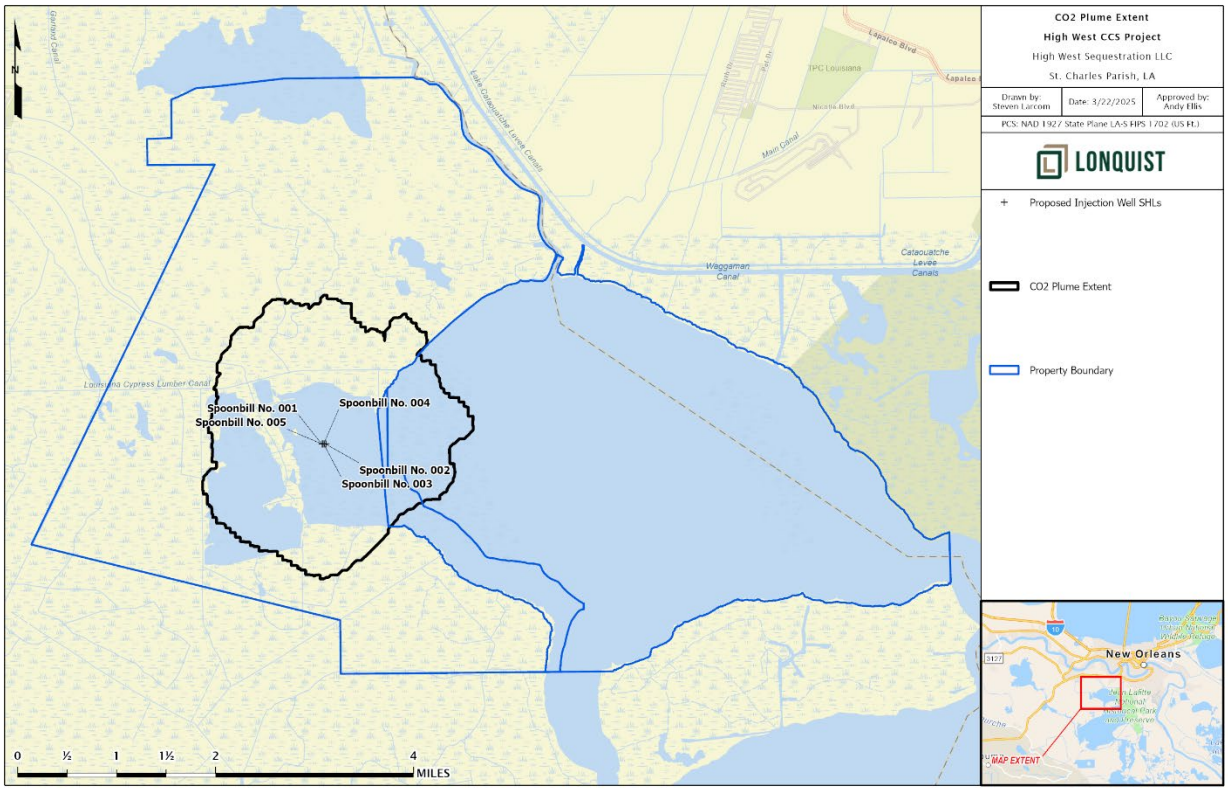

Figure 2-51 – Maximum CO_2 Plume Extent

2.7.2.1 Stabilized Plume Growth Analysis

Plume stabilization occurs when the growth rate or positional change has slowed to a nearly imperceptible change per year. At that point in time, the CO_2 plume is considered hydrodynamically trapped within the pore space. This stabilization point is determined by the model output, where the areal growth rate is less than 0.4% per year.

By the year 2073 (28 years post-injection), the plume is considered to be stable according to the results of the dynamic model. A significant reduction in growth can be seen at that time. After 2095, the areal growth rate decreases below 0.4% per year on average and will continue to decline. The carbon front's growth continues to steadily decline until the end of the model. Figure 2-51 shows the plume stabilizing within 50 years after injection operations.

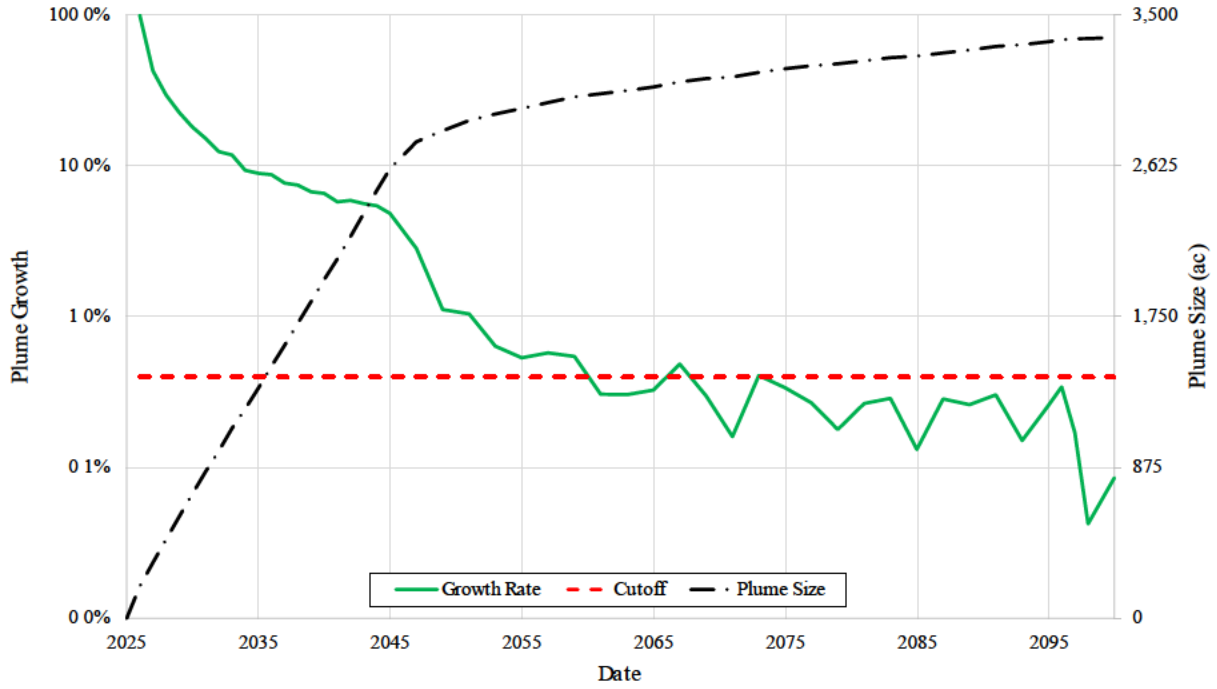

Figure 2-52 – Plume Growth Analysis

2.7.3 Critical Pressure Front for AOR Delineation

In accordance with SWO 29-N-6 **§3615.B** [40 CFR **§146.84**], the AOR was delineated by the critical pressure front created by injecting supercritical CO_2 into a saline aquifer. Critical pressure is the increase in reservoir pressure that may push in situ fluids out of the injection zone and into the lowermost USDW, in the presence of a bridging conduit such as an unplugged borehole. The initial step in predicting the pressure front involves calculating the critical threshold pressure for each completion stage. Subsequently, a numerical simulation is used to forecast the size and configuration of the critical pressure front.

A potential scenario for moving reservoir fluids to the USDW would be through an incorrectly plugged and abandoned wellbore that is open in both the top of the injection interval and the base of the USDW. The reservoir fluid would need to overcome the hydrostatic head of the mud column for any fluid to migrate out of the injection zone. In this case, it is assumed that the hypothetical well is filled with mud of a density equal to a 0.489 psi/ft (~9.4 pound per gallon) pressure gradient. Typical mud weights in this area are approximately 10 ppg or greater, therefore this value is a conservative assumption. The critical threshold pressure was calculated for each well where the top of injection ranges from 6,129 ft to 9,725 ft. The brine density is calculated to be 0.465 psi/ft based on a salinity of 125,000 ppm as discussed in Section 2.5.2.2.

(Eq. 4) $$P_{crit} = P_{mud} + P_{gel} - P_{initial}$$

The resulting critical pressure rise for the uppermost stage is a positive value. This positive value suggests that the reservoir pressure may be safely increased by approximately 157 psi without

risk of fluid migration to the USDW. Table 2-7 provides the critical pressure for each stage at the injection wells.

Table 2-7 – Critical Pressure by Completion Stage for the Injection Wells

Well No.	Reference Depth (ft)	Initial Reservoir Pressure (psi)	Critical Threshold Pressure (psi)
001	9,725	4,522	231
002	8,703	4,047	207
003	8,160	3,794	194
004	7,036	3,272	167
005	6,122	2,847	146

The critical pressure front is delineated based on the completion stage with the most significant pressure front, or a combination of pressure fronts from each completion. In practical terms, the critical pressure front is based on the greatest possible extent experienced in the model. The result is a pressure front that encompasses an area of 5,099 acres (~8 sq mi). The pressure front predominantly extends in the SWW-NEE orientation, reaching a maximum of 3.49 mi in diameter. Figure 2-52 shows a visual representation of the maximum extent of the critical pressure.

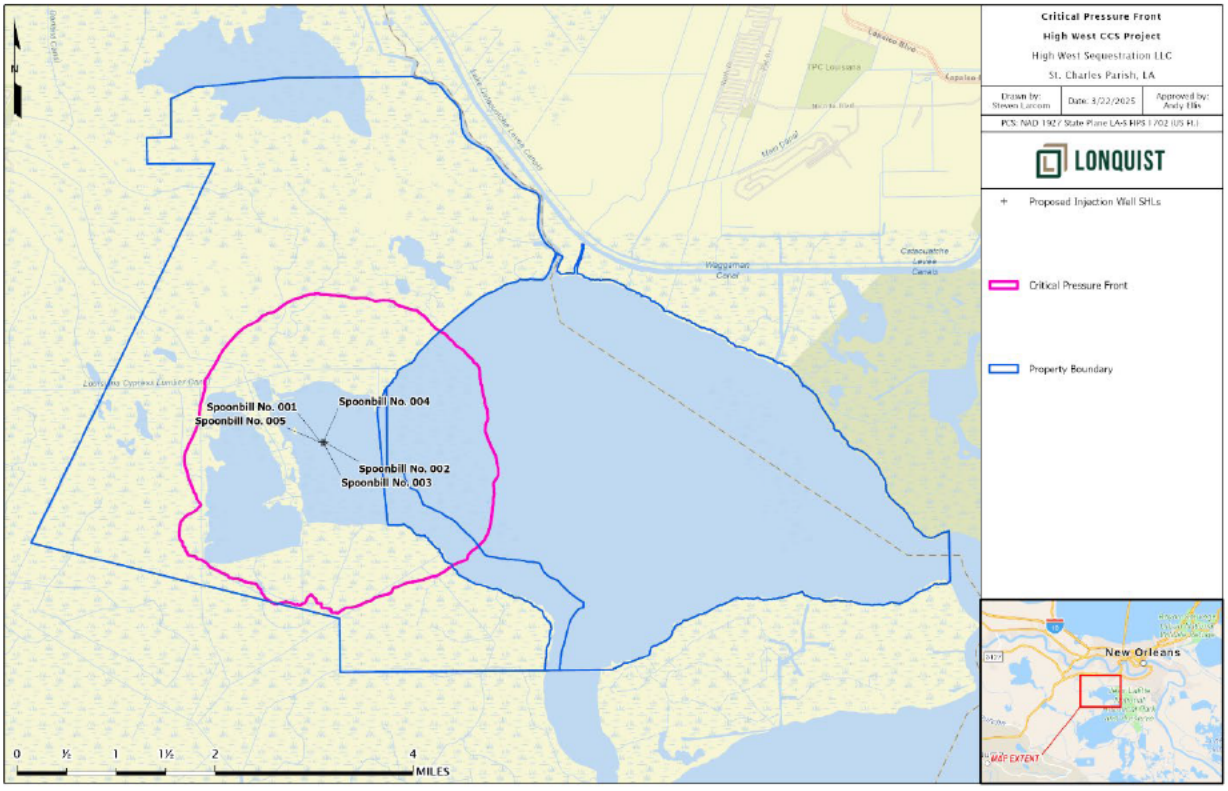

Figure 2-53 – Maximum Critical Pressure Front

2.8 Final AOR

The final AOR, based on 50 years after injection ceases and depicted in Figure 2-53, encompasses both the CO_2 and critical pressure fronts. Defining the monitoring requirements and potential corrective action plan for offset wells heavily depends on this designated AOR. As the AOR involves two distinct fronts, it is essential to consider specific monitoring and corrective action measures for each front, to ensure a thorough approach in managing the carbon sequestration project.

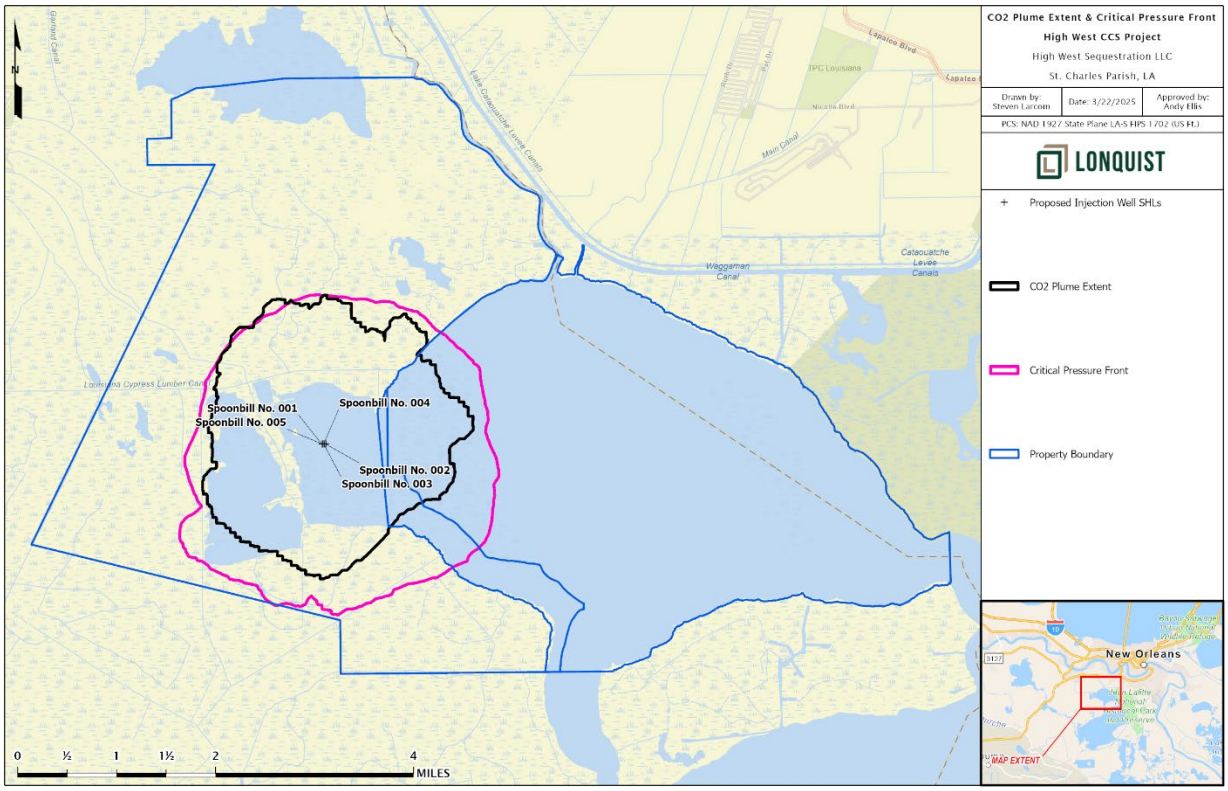

Figure 2-54 – Final AOR with CO_2 Plume Extent and Critical Pressure Fronts

Additional information to support Section 2 is provided in the following appendices:

Appendices

- App B-10 Well Logs Used in Static Model
- App B-11 - Static Earth Model Zone Values

2.9 References

Bachu, S. (2012). Drainage and Imbibition CO2/Brine Relative Permeability Curves at in Situ Conditions for Sandstone Formations in Western Canada. *Energy Procedia*, 37. 10.1016/j.egypro.2013.07.001.

Bachu, S., and Bennion, B. (2008). Effects of in-situ conditions on relative permeability characteristics of CO2-brine systems. *Environ Geol* 54, 1707–1722.

Backeberg, N., Iacoviello, F., Rittner, M. et al. (2017). Quantifying the anisotropy and tortuosity of permeable pathways in clay-rich mudstones using models based on X-ray tomography. *Scientific Reports*, 7. 10.1038/s41598-017-14810-1.

Beggs, D.H; J. P. Brill, J.P. A Study of Two-Phase Flow in Inclined Pipes. Journal of Petroleum Technology, 25 (May 1973)

Benson, S.; Pini, R.; Reynolds, C.; Krevor, S (2013). Relative Permeability Analysis to Describe Multi-Phase Flow in CO2 Storage Reservoirs; No. 2; Global CCS Institute: Melbourne, Australia.

Blondes, M. S., Gans, K. D., Engle, M. A. et al. (2018). U.S. Geological Survey National Produced Waters Geochemical Database (ver. 2.3, January 2018): U.S. Geological Survey data release. https://doi.org/10.5066/F7J964W8.

Carlson, D., and McCulloh, R. (2006). A Preliminary Examination of Geothermal Gradient throughout Louisiana's 64 Parishes. Gulf Coast Association of Geologic Societies Vol 56. 137.

Chen, X., Gao, S., Kianinejad, A., and DiCarlo, D. A. (2017). Steady-state supercritical CO2 and brine relative permeability in Berea sandstone at different temperature and pressure conditions. Water Resources Res., 53, 6312– 6321, doi:10.1002/2017WR020810

Eaton, B.A. (1968). Fracture Gradient Prediction and Its Application in Oil Field Operations. *Journal of Petroleum Technology*, 25-32.

Galloway, W.E., Hobday,D.X., and Magara,X., 1982,Frio Formation of the Texas Gulf Coast Basin— depositional systems, structural framework, and hydrocarbon origin, migration, distribution ,and exploration potential :The University of Texas at Austin, Bureau of Economic Geology Report of Investigations No. 122, 78 p

Hagedorn, A.R.; Brown, K.E. Experimental Study of Pressure Gradients Occurring During Continuous Two-Phase Flow in Small Diameter vertical Conduits. Journal of Petroleum Technology, 17 (April 1965).

Holtz, M.H. (2005). “Reservoir Characterization Applying Residual Gas Saturation Modeling, Example From the Starfak t1 Reservoir, Middle Miocene Gulf of Mexico.”

Hovorka, S. D., Holtz, M. H., Sakurai, S. et al. (2003). Frio pilot in CO2 sequestration in brine-bearing sandstones: The University of Texas at Austin, Bureau of Economic Geology, report to the Texas Commission on Environmental Quality to accompany a class V application for an experimental technology pilot injection well. *GCCC Digital Publication Series* #03-04.

Intergovernmental Panel on Climate Change (2005). IPCC Special Report: Carbon Dioxide Capture and Storage. Prepared by Working Group III of the Intergovernmental Panel on Climate Change. B. Metz, O. Davidson, H. de Coninck, M. Loos, and L. Meyer, eds. Cambridge, UK: Cambridge University Press.

Krevor, S. C. M., Pini, R., Zuo, L., and Benson, S. M. (2012). Relative permeability and trapping of CO2 and water in sandstone rocks at reservoir conditions. *Water Resources Res*.

McCain, W. D. (1991). Reservoir-Fluid Property Correlations—State of the Art. *SPE Res Eng* 6, 266–272. doi: https://doi.org/10.2118/18571-PA

Moody, L. An approximate Formula for Pipe Friction Factors. Transactions ASME, 69, 1005 (1947).

Molina, O., Vilarrasa, V., and Zeidouni, M. (2017). Geologic Carbon Storage for Shale Gas Recovery. *Energy Procedia*, 114. 5748-5760. 10.1016/j.egypro.2017.03.1713.

Newman, G. H. (1973). Pore-volume compressibility of consolidated, friable, and unconsolidated reservoir rocks under hydrostatic loading. *Journal of Petroleum Technology*, 25(02), 129–134. https://doi.org/10.2118/3835-pa.

Nicot, J., Oldenburg, C., Bryant, S., and Hovorka, S. (2008). Pressure perturbations from geologic carbon sequestration: Area-of-review boundaries and borehole leakage driving forces. *Energy Procedia*, 1, 47-54. https://doi.org/10.1016/j.egypro.2009.01.009.

Nielsen, L. C., Bourg, I. C., and Sposito, G. (2012). Predicting CO_2-water interfacial tension under pressure and temperature conditions of geologic CO_2 storage. *Geochimica et Cosmochimica Acta*, *81*, 28-38. https://doi.org/10.1016/j.gca.2011.12.018.

Noel, Tyler and Ambrose, W. A. 1985, Facies Architecture and Production Characteristics of Strandplain Reservoirs in the Frio Formation, Texas, The University of Texas at Austin, Bureau of Economic Geology Report of Investigations No. 146 p. 42

Peng, D. Y., & Robinson, D. B. (1976). A new two-constant equation of state. Industrial & Engineering Chemistry Fundamentals, 15(1), 59-64.

Snedden, J., and Galloway, W., 2019. The Gulf of Mexico Sedimentary Basin: depositional evolution and petroleum applications, Cambridge: Cambridge University Press, 326 p. https://doi.org/10.1017/9781108292795

Swanson, S. M., Karlsen, A. W., and Valentine, B. J. (2013). Geologic assessment of undiscovered oil and gas resources—Oligocene Frio and Anahuac Formations, United States Gulf of Mexico coastal plain and State waters: U.S. Geological Survey Open-File Report 2013–1257. http://dx.doi.org/10.3133/ofr20131257.

U.S. Environmental Protection Agency. (2013). Geologic Sequestration of Carbon Dioxide: Underground Injection Control (UIC) Program Class VI Well Area of Review and Corrective Action Guidance.

Vavra, C., Kaldi, J. G., and Sneider, R. M. (1992). Capillary Pressure. In: AAPG Methods in Exploration Series, No. 10: Development Geology Reference Manual (1992). D. Morton-Thompson and A. M. Woods, eds.

Y.-K. Li, L. X. Nghiem. Phase Equilibria of Oil, Gas and Water/Brine Mixtures from a Cubic Equation of State and Henry's Law. Canadian J. of Chemical Engineering, 64(3), 486 (1986).